JACS
JOURNAL OF THE AMERICAN CHEMICAL SOCIETY
pubs.acs.org/JACS

Article

Beyond-Kasha Photochemistry in a Heteroleptic Platinum−Dithiolene Complex

Michela Gazzetto, Flavia Artizzu, Salahuddin. S. Attar, Jakob T. Casanova, Luciano Marchiò, Luca Pilia, Antonio Monari, Paola Deplano,* and Andrea Cannizzo*

Cite This: https://doi.org/10.1021/jacs.6c00565

Read Online

ACCESS | Metrics & More | Article Recommendations | Supporting Information

ABSTRACT: Kasha's rule implies that photochemical reactions occur in the lowest excited state, regardless of excitation wavelength. Only a few chromophores have been reported to exhibit efficient non-Kasha responses. While these are rare, their exploitation could revolutionize multiresponsive materials, improve solar energy utilization, and advance light-driven chemical reactions. Studying non-Kasha dynamics enhances the understanding of excited-state processes and could broaden the range of usable chromophores in real applications. This article focuses on the anionic heteroleptic dithiolene complex $[Pt((R)\text{-}\alpha\text{-MBAdto})(quinoxdt)]^-$ ((*R*)-*α*-MBAdto = (*R*)-(+)*α*-methylbenzyl-dithiooxamidate; quinoxdt = [1,4]dithiino[2,3-*b*]quinoxaline-2,3-bis(thiolate)) in acetonitrile, which undergoes long-lived conformational changes exclusively upon excitation of higher excited states. In its tight ion-pair adduct with HCl, these changes drive HCl detachment within 70 ps, trigger a dramatic blue-shift in the S_1-S_0 gap, and lead to aggregate formation. Although these processes ultimately occur in the lowest excited state, they rely on non-Kasha isomerization, representing a "beyond-Kasha" process. Such systems pave the way for innovative multiresponsive materials and non-Kasha excitation-dependent photochemical applications.

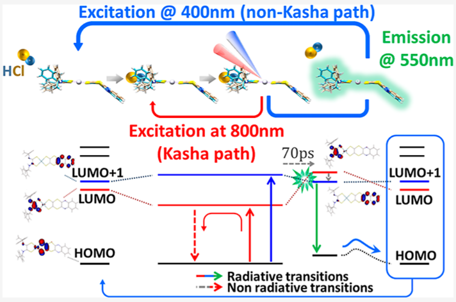

INTRODUCTION

Kasha's rule states, when adapted to photochemistry, that photochemical reactions in the condensed phase occur appreciably only in the lowest excited state of a given multiplicity, irrespective of the excitation wavelength (λ_{Exc}). It affects any aspect of photochemistry and sets severe limitations to the efficiency of solar energy usage, e.g., for photocatalysis, or to controlling, not just triggering, chemical reactions using light. It also opposes the development of multiresponsive materials, whose light response could depend on the λ_{Exc} or on the number of excitations. Some of its violations are known[1,2] and are extremely interesting for applications in the domain of multiresponsive photoactive materials,[3] dual-emission probes,[2,4] or efficient photon-energy utilization.[5] Moreover, studying molecules showing a non-Kasha (nK), also called anti-Kasha,[2,4] behavior can allow investigating relaxation mechanisms and molecular processes on, or from, higher excited states, benefiting the comprehension of fundamental molecular phenomena and the improvement of computational quantum chemistry approaches.[6] Thanks to ultrafast spectroscopies and advances in excited-state computational methods, further evidence of the Kasha's rule violation has been reported for the major types of excited-state reactions as photoisomerization, bond-breaking, and charge and energy transfers, raising a growing interest in nK photochemistry.[2,7] However, only a few classes of chromophores, as azulene and their derivatives, Zn porphyrins, and some metal complexes,[2] feature an nK response efficiently exploitable in real applications. A huge potential could be unleashed by increasing the classes of chromophores for nK applications.

Recently, a nK behavior was observed in d^8-metal dithiolene complexes (MCs), both homoleptic[8] and heteroleptic,[9,10] containing the quinoxdt ([1,4]dithiino[2,3-*b*]quinoxaline-2,3-bis(thiolate)) ligand where the quinoxaline ring (quinox) is connected to the dithiolate C2S2 moiety through a 1,4-dithiine bridge.

These MCs[8,9] in solution have been investigated with ultrafast spectroscopy,[11,12] and an outstandingly long lifetime (1−2 ps) of the second singlet excited state (S_2),[11] comparable with the higher excited states lifetime in Zn porphyrins, was observed. This uncommon condition allows these MCs to emit detectable nK emission. Such an exceptionally slow internal conversion (IC) was rationalized as due to the fact that the first and second excited states have profoundly different electronic density distributions, with no overlap between the orbitals involved in the IC process (see Figure 1B and S1C). This

Received: January 9, 2026
Revised: February 23, 2026
Accepted: February 25, 2026

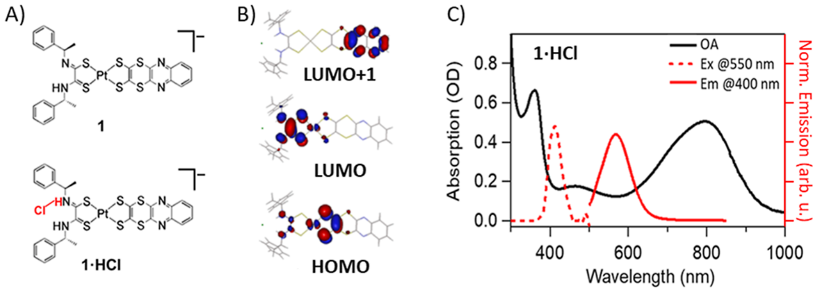

Figure 1. (A) Structural formulas of the precursor (**1**), namely, the parent molecule before adding HCl, and its HCl adduct (**1·HCl**). (B) DFT calculated molecular orbitals of **1·HCl**. (C) Steady-state absorption (OA, black line), non-Kasha emission excited at 400 nm (Em@400 nm, red solid line), and an excitation spectrum detected at 550 nm (Ex@550 nm, red dashed line) of **1·HCl** in acetonitrile. See the Supporting Information, Section SI.2, for more details.

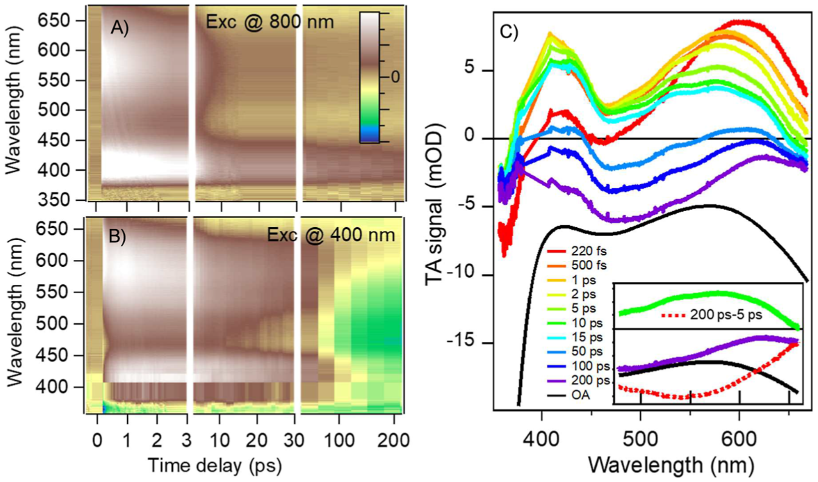

Figure 2. Transient absorption (TA) measurements upon (A) excitation at λ_{Exc} = 800 nm (B) and 400 nm. (C) Representative selection of TA spectra at different time delays from panel B. For the sake of comparison, the steady-state absorption band is shown inverted and suitably normalized. In the inset are shown the difference spectra between the TA spectra at 5 ps (green) and 200 ps (violet) to isolate the spectrum of the emission at 550 nm (dashed red line).

different electron density localization makes the IC a long-range charge transfer (CT) process between the quinoxdt and the other ligand, characterized by a large reorganization energy. This condition dramatically slows the IC down.[10]

Remarkably, the heteroleptic complex [Pt((*R*)-*α*-MBAdto)-(quinoxdt)]$^-$ (**1**), where (*R*)-*α*-MBAdto = (*R*)-(+)*α*-methylbenzyl-dithiooxamidate (Figure 1A), undergoes photoisomerization, which is triggered only upon excitation of S_2 and, after the IC process toward the first singlet excited state (S_1), continues to evolve. This process shows a high quantum yield (QY), is reversible, and is long-lived (at least ns).[11]

By HCl addition, **1** forms a 1:1 adduct (**1·HCl**, Figure 1A), which still preserves the nK behavior, despite its optical properties are dramatically changed.[8,9] This motivated us to investigate also the nK dynamics of **1·HCl** with ultrafast transient absorption (TA) spectroscopy to understand whether and how the nK isomerization is affected by the **1·HCl** formation and to verify whether the CT character of the IC still applies. Eventually, these results may help to design new molecules with an enhanced nK emission QY.

The results reported in this study reveal that only the nK excitation can induce the breaking of the adduct with the release of HCl in tens of ps. We rationalize this observation as an effect of nK photoisomerization, which triggers a destabilization of **1·HCl** in acetonitrile. All the molecules undergo this reaction, as proved by the strong TA signals related to this process. Therefore, the system herein investigated can be considered the archetype of a new family of efficient multiresponsive materials which exploit the nK photoisomerization to achieve an excitation-dependent photochemical response. These results represent a proof of concept for new strategies based on selective triggering of photoisomerization, exploitable in the emerging field of nK photochemistry, where, so far, the dominant approach relies on increasing the higher excited-state lifetime to make the functional process competitive.[2]

■ RESULTS AND DISCUSSION

All the measurement in this article are carried out in acetonitrile. Figure 1C shows the steady-state UV−vis optical absorption, emission (λ_{EXC} = 400 nm), and excitation (λ_{Em} = 550 nm) spectra of **1·HCl**. The nK 550 nm emission[10] is observed only upon HCl addition and with low QY ($\lesssim 10^{-3}$), whereas no emission is observed exciting the lowest absorption band at 800 nm. The latter speaks for a strongly quenched fluorescence with a sub*μs* lifetime.

As aforesaid, the $S_2 \rightarrow S_1$ IC in **1** is astonishingly slow (~1 ps against typically ~10 fs)[11] because the IC is a CT process associated with a remarkable change in the electronic distribution between the LUMO + 1 and the LUMO orbitals (Figure S1).[9] This unusual condition makes the S_2 emission detectable.

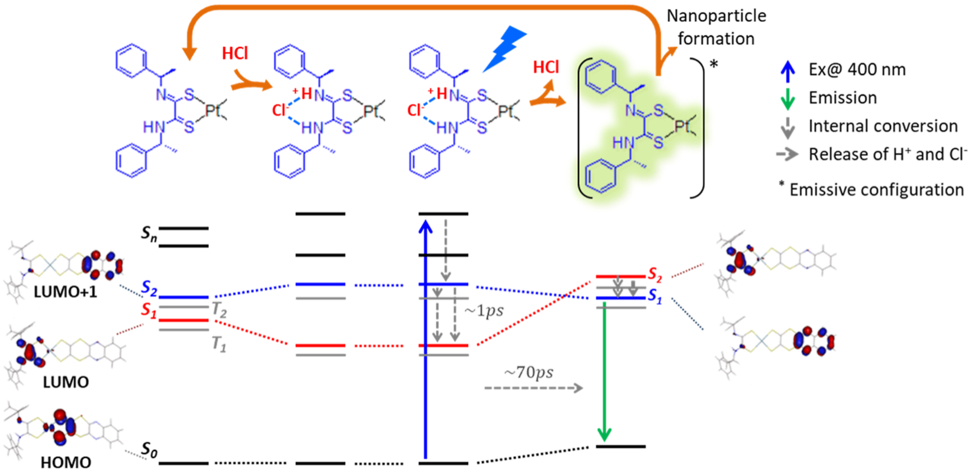

Figure 3. Full photocycle triggered by the 400 nm excitation and the effect of the HCl addition on the energetics (bottom). The top row shows the corresponding structural configurations. The relaxation toward the lowest excited state S_1 involves a long-lived (~1 ps) higher excited state S_2. Upon HCl release in ~70 ps (69 ± 3 ps from Figure S14), the system relaxes into an emissive configuration where the excited electron density is centered on the quinoxdt ligand (Figure S12 and relative discussion), from which it can relax back to the ground state or trigger aggregation. Both the 1 ps and the 70 ps relaxations are accompanied by conformational dynamics (a tentative conformational change is shown in Figure S12). To show the excited electron distribution, the involved molecular orbitals are drawn. For the sake of completeness also, the lowest triple states are shown; however, since the transient configurations are unknown, their relative position is tentative. Molecular orbitals and structures adapted from ref 9, copyright 2017 American Chemical Society.

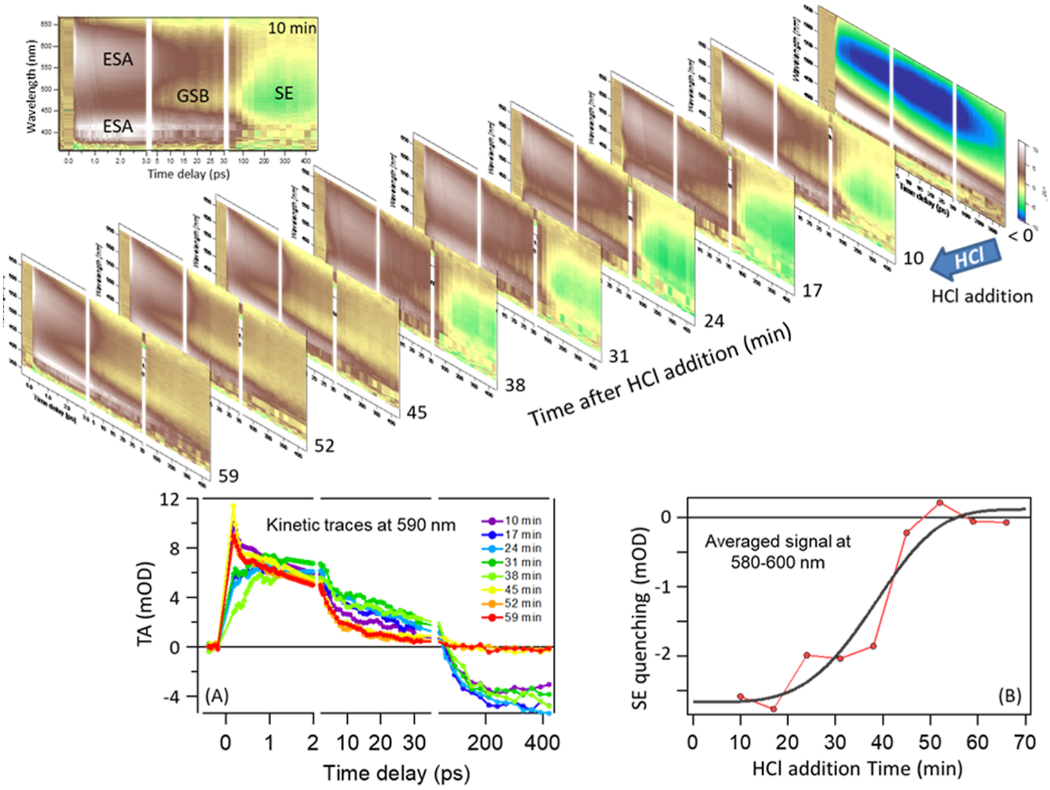

Figure 4. Main figure: a series of consecutive TA scans as a function of time after the addition of HCl. The first plot (<0) shows the signal of complex **1** (see ref 11). The strong negative (blue) signal corresponds to the ground-state bleach (GSB). For clarity, the signals of **1·HCl** (ESA, excited-state absorption, SE, stimulated emission) are marked in the first scan after HCl addition (10 min). Inset (A) Kinetic traces at 590 nm (where essentially SE only is monitored and there is no contribution from GSB) at subsequent times after HCl addition. Inset (B) SE quenching kinetics monitored as the amplitude of TA signal at 400 ps (the longest scanned delay time) averaging points between 580 and 600 nm, where the TA signal is mainly SE. The solid line is obtained by fitting the data to eq 1. Kinetic traces at other wavelengths are shown in Figure S9. The reported addition times correspond to the end of each scan, which lasts 7 min each and that after HCl addition, we waited 3 min for complete, homogeneous **1·HCl** formation. The sample was continuously exposed to 1 kHz 400 nm irradiation from minute 3 to 59.

Before investigating the nK dynamics of **1·HCl**, we characterized the relaxations upon excitation of the lowest electronic transition (Figure 2A). We observe the same behavior (see the Supporting Information for details) of **1** upon excitation of $\boldsymbol{S_1}$,[11] namely: a 0.9 ps vibrational cooling followed by a 3.9 ps intersystem crossing (ISC) toward long-lived low-lying triplet states. This implies that the **1·HCl** formation has no effect on the $\boldsymbol{S_1}$ dynamics. It is worth noting that both **1·HCl** and **1** do not show any emission upon excitation of the lowest absorption band.

Conversely, adding HCl profoundly changes the TA signal (Figure 2B,C) upon excitation of the nK transition at 400 nm. The most striking result is the formation of a negative signal after 50 ps between 450 and 600 nm, which sits on top of the positive excited-state absorption (ESA) signals present from the very beginning. To isolate this contribution, we subtracted from a long-lived spectrum (200 ps) an early time spectrum (5 ps), revealing a negative signal centered at 550 nm (the red dashed line in the inset of Figure 2C). We chose 5 ps because it is late enough to assume vibrational relaxation and cooling dynamics completed but early enough to exclude contamination from the negative signal. The comparison of this isolated contribution with the steady-state emission in Figure 1C confirms that this signal is due to the stimulated emission (SE) corresponding to the nK emission. This emission is fully allowed since its amplitude is comparable with the ground-state bleach (GSB) one, and at least ns lived, lasting well beyond the investigated temporal window (up to 450 ps). This result is unexpected and somehow astonishing.

It is unexpected because a fully allowed (i.e., an expected radiative time of tens of ns) and long-lived emission (i.e., a total lifetime between few ns and the radiative time) should have an emission QY at least of 10^{-1}, whereas the reported value[9] is $<10^{-3}$. It is astonishing because this allowed emission (therefore stemming from a singlet state) develops on a so long-time scale, ~70 ps, that all the electronic and vibrational relaxation can be considered concluded, and λ_{Exc} should no longer play any role. However, upon direct excitation of $\boldsymbol{S_1}$ at 800 nm, no emission is observed (Figure 2A).

To rationalize such unpredictable behavior, we need first to identify the electronic state populated after the 400 nm excitation and before the emission rise. The comparison with the TA signals excited at 800 nm (Figure S5) reveals that ESA and GSB bands excited at 400 and 800 nm in the first 10 ps are practically the same, showing that after the subpicosecond dynamics, **1·HCl** reaches the same excited state. However, upon 400 nm excitation, we observe a subpicosecond rise absent in the signal excited at 800 nm (Figure S6), which shows a more complex and faster picosecond evolution than the 400 nm one (Figure S7). Accordingly, we can conclude that upon 400 nm excitation, we populate the same electronic state excited at 800 nm, i.e., $\boldsymbol{S_1}$, after an IC process lasting ~1 ps (see the central part of Figure 3 for the photocycle describing the firsts ps). As for **1**,[11] where a 1.4 ps $S_2 \rightarrow S_1$ IC was reported, we explain it as an effect of the LUMO−LUMO + 1 spatial separation (Figure 3). However, since in **1·HCl** nK emission rises in 10 s of ps and lasts ns, it cannot originate from higher excited states lasting few ps.

A convincing explanation requires reconsidering how the emission QY, which is $<10^{-3}$,[9,10] was estimated. As aforesaid, results in Figure 2 contradict such a low value, implying QY > 10^{-1} and speaking for a quenching process in steady-state measurements, absent in a time-resolved experiment. The striking difference is that in steady-state measurements, a cuvette without circulation is used, and the molecules are excited multiple times. Conversely, the latter uses circulated solutions, with pump fluence and sample volume chosen to excite only a few percent of molecules during acquisition. To verify whether this is the cause, we ran consecutive TA experiments on a small volume (2 mL of solution with concentration $c = 4.43 \times 10^{-4}$ M) to reduce the solution buffer effect and with faster acquisition parameters (7 min for each experiment) to monitor possible photodegradation processes (Figure 4). Consistent with the first experiment (Figure 2), we initially observed the same emission. After 40 min, this emission is nearly fully quenched (inset A, Figure 4) but with a sigmoidal (inset B, Figure 4) rather than monoexponential decay, as expected for one photon degradation processes. Remarkably, after the SE quenching kinetics are completed, a negative signal, ~100 times smaller than SE in the fresh sample, is observed exclusively upon 400 nm excitation (Figure S8). This implies a 10^{-3} emission QY, in excellent agreement with the literature.[9,10]

Moving to the S-shaped kinetics, this is more characteristic of phase transformations upon nucleation and, assuming constant nucleation rate and temperature, a three-dimensional growth follows the Avrami equation:[13]

$$R_{\mathrm{V}} = 1 - e^{-Kt_{\mathrm{ncl}}^{4}}(t_{\mathrm{ncl}} > 0) \tag{1}$$

where R_{V} is the volume fraction of the final phase at nucleation time t_{ncl} and K is a constant proportional to the formation rate of nucleation centers and volume growth rate of the transformed material. As tacitly assumed in inset B of Figure 4, the SE amplitude, estimated as the TA amplitude at 590 nm, at the longest scanned time delay reports on R_{v} at a given t_{irr}:

$$R_{\mathrm{V}} = \frac{\mathrm{TA}_{590\mathrm{nm}}^{400\mathrm{ps}}(t_{\mathrm{irr}}) - \mathrm{TA}_{590\mathrm{nm}}^{400\mathrm{ps}}(0)}{\mathrm{TA}_{590\mathrm{nm}}^{400\mathrm{ps}}(\infty) - \mathrm{TA}_{590\mathrm{nm}}^{400\mathrm{ps}}(0)} \tag{2}$$

where we consider the differential change because of the small long-lasting residual (although constituting <3% of the overall change). Data are indeed perfectly described by eq 1, corroborating the formation of a solid upon 3D heterogeneous nucleation as quenching mechanism (fitting coefficients in Table S3). As countercheck, we exposed a sample to steady-state 400 nm radiation, and indeed a dark green, nonemissive precipitate was formed (Figure S2B). To verify whether the aggregated molecules were photodamaged, we added NH_3 to the mixture. Indeed, since NH_3 can withdraw HCl from the adduct,[9] and **1** is more soluble than **1·HCl**, the HCl-deprived precipitate can be redissolved. The resulting solution shows the same spectroscopic features as the freshly prepared sample, including the changes upon HCl addition. This definitively confirms that the quenching mechanism involves intact, unexcited **1·HCl** adducts and, to a lesser extent, molecules of **1** from de-excited adducts, discarding photodegradation and photofragmentation. With our fluence (3×10^{13} absorbed photons per second) and solute content (5×10^{17} molecules), the fraction of adducts that were excited, at least once, before the near-complete suppression of SE ($t_{\mathrm{irr}} = 40$ min) is less than 15% (see the Supporting Information). Therefore, when the suppression of SE, which involves the majority of **1·HCl**, is observed, only about 15% of them have been excited. This implies that the quenching of SE is not caused by the depletion of the concentration of **1·HCl**. Instead, most of the aggregated molecules have never been excited and still bear HCl. Since the first step of nucleation is still diffusion limited, it should occur at μs times or longer, therefore involving de-excited molecules. The formation of aggregates of unexcited adducts is a fact, as observed in solutions stored in the dark for days. This indicates that **1·HCl** can aggregate thermally, although inefficiently, at room temperature. Unexpectedly, de-excited molecules accelerate aggregation from days to minutes. Since photoexcitation induces conformational changes, as observed in **1**,[11] and significantly speeds up nanoparticle formation, we infer that the latter requires a specific configuration, achieved either thermally with low probability or efficiently through photoexcitation. The aggregate consists of nanoparticles because the circulated sample remained clear and with no scattering, allowing to exclude particles larger than hundreds of nm. Spectroscopic stability was also confirmed (Figure S10). These findings imply that de-excited molecules act as nucleation centers. Their configuration, different from the ones accessible from S_1 and the S_0, facilitates the initial cluster formation, thus representing heterogeneous nucleation, even though the seeds are chemically similar to the solute.

Quenching kinetics reveal that nK emission activation is inhibited in the solid. As further evidence, we found that the emission was undetectable at cryogenic temperatures, where the sample was a glassy matrix. These findings indicate a process requiring molecular mobility, such as photodetachment or photoinduced recombination, rather than solely intramolecular relaxations (in the latter case, we should even expect an increase of the emission at cryogenic temperatures). The 70 ps rise time of the emission is too fast for diffusional mechanisms, ruling out photoinduced recombination. We can also rule out any effect due to a variation of HCl concentration in solution because spectra were measured in an HCl excess (10 mM of HCl and 0.4 mM of solute); therefore, even if all the **1·HCl** would release HCl, the total HCl concentration change would be 4% at most.

The fact that the direct excitation of S_1 does not induce SE and (fast) aggregation, whereas the S_2 excitation does, unveils that the conformational change responsible of such different photochemical behavior is triggered during the short-lived non-Kasha state and continues to evolve after the IC to S_1. To identify the nature of the process induced by this photoisomerization, we observe that the emission must stem from S_1, which, however, would naturally emit at $\lambda > 800$ nm. The only process able to explain a so dramatic blue-shift is the opposite process which caused the decrease of the $\mathbf{S_0{-}S_1}$ gap and the red-shifting of the steady-state absorption bands upon HCl addition: breaking of the adduct **1·HCl** with ejection of an HCl molecule. Indeed, as can be seen experimentally and computationally (Figure S1), the HCl release causes a blue-shift of almost 200 nm (from ca. 800 nm to 600 nm) of the lowest optical transitions. Ejection of Cl^- alone is excluded by TD-DFT calculations (see ref 9 and Figure S1C), in agreement with previous findings on similar tight ion-pair adducts which lose HCl instead of Cl^-.[14] Noteworthily, we observed a monoexponential SE rise with no evidence of intermediate processes (see Figure S14 and related discussion), supporting a dissociation process of the whole HCl molecule.

Thus, this study represents a rare case of non-Kasha photochemistry, rather than photophysics, where femtosecond processes initiate effects lasting hundreds of picoseconds to nanoseconds: in subpicosecond time scales: the S_2 excitation in **1·HCl** destabilizes the contact-pair site, leading to HCl detachment within tens of ps. The complex after the HCL release is chemically equivalent to **1** but differs from it, as it can trigger aggregation likely in μs and exhibit strong emission, both absent in **1**. It is worth mentioning that the formation of micro- and nanometric aggregates of HCl adducts of a platinum-bis-dithiooxamidate complex was earlier observed by Lanza, Campagna, and co-workers.[15]

Precipitate formation is the final step of a process beginning with the growth of nanosized particles, which stay in solution because of their small size and continuous flow. Therefore, the content of molecules before and after nucleation remains unchanged, explaining why the signal intensity in the first 10 ps is independent of nucleation (Figure 4). This proves that molecules in solid phase and solution are the same, and only after HCl ejection do the latter differ from the former. For these reasons, we previously stated that the aggregation needs photoisomerized molecules as seeds, but it contains nonexcited **1·HCl**.

We can therefore conclude that adducts **1·HCl** are not emissive, but the HCl photodetachment converts them into emissive species, with the "non-Kasha" emission originating from $\mathbf{S_1}$. In this respect, it could also be described as nK photoinduced chemiluminescence, resulting from a chemical reaction happening or triggered in higher excited states. Accordingly, the emission quenching is caused by the depletion of free **1·HCl** by incorporation into aggregates, which are nonfluorescent because the HCl photodetachment is inhibited.

About the emissive behavior, direct excitation of S_1 of **1·HCl** shows no steady-state emission due to competitive ISC;[11,16] therefore, since the HCl release makes the system emissive, it must also drastically reduce the ISC rates. This definitively points to a conformational change that would allow for strong emission. An extensive computational study is in progress to clarify the details of structural dynamics, but preliminary results reported in Section SI.8 (Figures S11 and S12 and related discussion) confirm that these systems have complex potential energy surfaces with different stable local minima,[11] thermally and optically accessible. Importantly, we do not pretend to report a fully computational description of all the complex photophysical and photochemistry pathways, which would be out of the scope of the present contribution, but rather provide some argument to substantiate the previously sketched mechanism. Relevant here is that one of these minima, close to the equilibrium configuration and thermally connected to it, exhibits inversion of LUMO and LUMO + 1 with respect to the absolute minimum (Figure 3). This is plausible because in **1** these MOs are almost degenerate and even inverted in vacuum.[11] This configuration is shown in Figure S12. The excited electron density of the charge transfer state S_1, after HCl ejection, would be exclusively localized on the quinoxdt centered LUMO moiety, without relevant Pt orbital contributions (Figure 3). This condition could increase the π-staking interaction of this ligand, explaining the initial aggregation. Furthermore, the suppression of Pt contribution, negligible overlap between the orbitals occupied by the excited electron and the hole, and the same π symmetry of these two singly occupied orbitals (which would make ISC forbidden) could drastically reduce the spin−orbit coupling, thereby accounting for the emissive behavior of the photoisomerized complex. This is supported by the preliminary calculations reported in Section SI.8 of the Supporting Information (Tables S7−S9, and relative discussion), where we also note that the S_2 is quasi degenerated with several higher triplet states, with the closest triplet state being at ca. 90 cm^{-1}. Remarkably, upon 400 nm excitation, the sample after 59 min of irradiation produces TA signals similar to the 800 nm excitation (Figure S8), except for a small long-lived negative signal at 500−600 nm. This means that when HCl cannot be released, adducts follow the proposed nK emission mechanism of **1**. Concerning the long-lived signal, its presence is confirmed by nanosecond time-resolved measurements on photoaggregated **1·HCl** (Figure S2A). This suggests that the long-lived signals arise from a small fraction of **1·HCl** in the aggregate that can still release HCl, as for instance on the surface or in voids (or less dense regions) of the aggregates or a small fraction of **1·HCl** dissociated from the aggregates. Very likely, these adducts can undergo geminate (in the voids) or nongeminate (on the surface or in solution) recombination, giving a constant signal over time.

These preliminary computational results also help identify possible conformational changes that could transform photoexcited molecules into nucleation centers and promote the stacking of unexcited molecules. In particular, the local minimum configuration that is thermally accessible from the global minimum (Figure S12 and related discussion) is the most plausible candidate for the isomer responsible for precipitate formation. In this conformation, the two benzyl rings in the dithiooxamidate moiety are oriented more parallelly and ordered, which could facilitate the formation of packed and ordered aggregates and ultimately of nanoparticles.

Before concluding this section, we should comment on the involvement of triplet states in the nK emission. Due to heavy atom effects, on the tens-of-ps to ns time scale, triplet states are very likely populated,[11] as also supported by the calculated spin−orbit coupling (Tables S7−S9, and relative discussion). This could allow for an indirect mechanism of delayed fluorescence, where the emissive state is repopulated from the triplet (dark) states. However, as detailed in the Supporting Information (SI.10), even if we cannot exclude such a process, it would not alter the main conclusion that our experimental results speak for an allowed transition with a long lifetime.

■ CONCLUSIONS

In this study, the intriguing photochemical properties of the **1·HCl** adduct are presented, complementing our previous work without HCl. We demonstrated that the excitation of long-lived (∼1 ps) higher excited states triggers conformational changes. They continue to evolve after the IC to S_1 and to long-lived triplet states, as already observed in **1**,[11] and can trigger high-yield chemical reactions. Therefore, the system investigated herein is the archetype of a new promising family of efficient multiresponsive materials, leveraging non-Kasha photoisomerization for excitation-dependent photochemical responses. Different mechanics of different nature concur to define the photochemical properties of the system: (1) a non-Kasha photoinduced chemiluminescence and (2) molecular aggregation upon nucleation with the photoexcited molecules themselves acting as nucleation centers.

The "non-Kasha" chemiluminescence is caused by the HCl detachment on ∼70 ps, triggered by subps conformational changes occurring in the higher excited states. This veritable non-Kasha chemical reaction triggers a dramatic S_1−S_0 blue-shift and brings the molecule toward a configuration, which is emissive and responsible of turning photoexcited molecules into a nucleation center for unexcited molecules. This causes initially the formation of nanoparticles and eventually a precipitate. In this phase, molecules cannot release HCl and remain nonemissive (QY $\sim 10^{-3}$), in contrast to non-Kasha photoinduced chemiluminescence (QY $> 10^{-1}$).

This result is groundbreaking for several reasons: (1) it is the first evidence of nonintramolecular photochemical reaction selectively induced by non-Kasha excitation with high yield, (2) it demonstrates that fs and subps dynamics can drive processes on much longer time scales not only in biomolecules, and (3) this way to exploit a non-Kasha response represents a radical change of view, paving the way to the emerging field of a veritable non-Kasha photochemistry.[2] Unlike the aforementioned prevailing approaches, the functional photoprocess (HCl release) occurs on the long-lived first excited state, modified by non-Kasha photoisomerization. We introduced the term "beyond-Kasha photochemistry" to emphasize this special situation where we can switch between "Kasha" reactions (namely, occurring on the lowest excited state of a given multiplicity) by non-Kasha changes.

These results open new aspects to investigate, as identifying the nK conformers, the relevant features of the singlet and of triplet potentials energy surfaces and the formation and growing mechanisms of the molecular solid. It would also be worth investigating the capability of the solvent to modulate the nK activity, and the presence of specific low-frequency modes, vibrationally coupled to modes enabling HCl dissociation and further conformational changes, which could be populated upon relaxation toward $\mathbf{S_1}$. Before concluding, it is worthy of notice that although the experimental evidence and the computational data reported here allow us to derive our interpretations, they do not allow us to draw conclusions about the specific deactivation paths and therefore about some of the fundamental mechanics underlying the observed processes. Indeed, in metal complexes, the relaxation of high-energy excited states can involve ultrafast ISC and even recrossing between states of different spin multiplicities, processes that might populate long-lived, high-energy singlet or triplet states. In this respect, the rather strong values of spin−orbit couplings reported in the SI speak to an important role of the triplet states in defining the deactivation paths. For such a thoughtful investigation, a nonadiabatic computational approach is mandatory to identify the possible conformers, the relaxation paths from the different excited states, and the role of external parameters, as the solvent and the specific acid. This extensive computational study, which is out of the scope of this review, is ongoing.

■ MATERIALS AND METHODS

Sample Preparation

The complex *n*-Bu$_4$N[Pt((*R*)-*α*-MBAdto)(quinoxdt)] (*n*-Bu$_4$N[**1**]) was synthesized and characterized as described in ref 9. The solvent used for optical measurements was acetonitrile of spectroscopic quality. 2 mL of solution was prepared with concentration $c = 4.4 \times 10^{-4}$ M, corresponding to an optical density of 0.1 OD at 800 nm and 0.04OD at 400 nm in 200 μm. To form the **1·HCl** adduct, a solution of 10 mM of HCl in acetonitrile was added to the solution of complex **1**, until a [**1**]/[HCl] ratio of 1:3 was reached. The effect of HCl addition on the optical spectra is discussed in ref 9 and summarized for convenience in the Supporting Information.

Optical Characterization

The UV−vis−NIR absorption spectra of **1·HCl** in acetonitrile solution were acquired with an Agilent Cary 5000 spectrophotometer using a 10 mm path length quartz cuvette. Emission and excitation spectra were collected with an Edinburgh Instruments FLS1000 photoluminescence setup equipped with extended PMT980 and nitrogen-cooled PMT1700 photomultiplier tubes. A 450 W CW xenon lamp was used for steady-state spectra. Time-Correlated Single

Photon Counting (TCSPC) measurements were performed by using a pulsed 375 nm EPL laser (average power 150 μW, repetition rate 20 MHz, and pulse width 75 ps) on a freshly prepared solution in acetonitrile. Data were acquired after 10 min of accumulation. After the measurement, the incipient formation of a precipitate was noted.

TA Measurement

The setup is described in detail in the Supporting Information and ref 17. Shortly, it is an ultrafast transient absorption (TA) setup with single-shot referenced detection operated with a 1 kHz femtosecond pulsed laser source (fundamental at 800 nm, 10 nm bandwidth, and 100 fs pulse length). Samples were excited at 800 nm (100 nJ/pulse into 60 μm diameter spots), close to the maximum of the lowest absorption band, and at 400 nm (65 nJ/pulse into 60 μm diameter spots), close to the maximum of the excitation band responsible of the 550 nm non-Kasha emission (Figure 1). With this setup configuration, a whole time-wavelength TA 2D plot (TA spectra at different time delays) with an acceptable signal-to-noise ratio was obtained in ca. 7 min. A power dependence measurement of the pump was regularly carried out before data acquisition to ensure that experiments were conducted in a linear absorption regime. After correction for probe group velocity dispersion, data from −180 fs to +180 fs around time zero were neglected to avoid artifacts caused by pump−probe cross-phase modulation from the solvent (see the Supporting Information).

Solutions were circulated in a closed flow circuit through a UV-grade flow-cell with a 200 μm-thick channel. The flow speed was set to 60 μL/s, which allows operating in a single-shot per spot regime to prevent signal artifacts and sample photodegradation due to multiple excitations and photoaccumulation. The TA experiments were always carried out on freshly prepared samples, with and without HCl addition (in the text, **1·HCl** and **1**, respectively).

In an aprotic solvent, such as acetonitrile, the HCl molecule is not expected to be dissociated. Moreover, these adducts can lose HCl instead of Cl^- since the hydrogen atom is more strongly linked to the chloride ion in comparison with the amidic nitrogen one.[14] This implies that very likely the adduct formation is not a two-step process but involves an interaction between the complex and a whole, undissociated HCl molecule. More relevant for this study, this also guaranties us that the sample is not a mixture of only protonated **1** and **1·HCl** but it is only made of the latter.

To point out and monitor photoaccumulated effects, a small volume (2 mL) of **1** solution was placed in the setup, and HCl was added in situ. To have a uniform addition, the sample was circulated in the dark for 2 min. After the check for excitation linearity (~1 min), 8 consecutive sets of experiments were acquired upon 400 nm excitation.

■ ASSOCIATED CONTENT

SI Supporting Information

The Supporting information is available free of charge at https://pubs.acs.org/doi/10.1021/jacs.6c00565.

> Transient absorption setup; effects of HCl addition; photocycle upon 800 nm excitation; comparison of the earlier transient absorption signal upon 800 and 400 nm excitations; comparison of the TA signals of the fresh sample upon 800 nm excitation and of a photoexposed sample upon 400 nm excitation; fitting of the quenching kinetics with the Avrami equation; calculation of the fraction of excited molecules; preliminary results from calculations; global fit analysis of the traces from panel A of Figure 4; and comment on the involvement of triplet states in the non-Kasha emission (PDF)

■ AUTHOR INFORMATION

Corresponding Authors

Paola Deplano − *Dipartimento di Scienze Chimiche e Geologiche, Università di Cagliari, Cagliari I-09042, Italy;* Present Address: Dipartimento di Ingegneria Civile, Ambientale e Architettura, University of Cagliari, I-09123 Cagliari, Italy (P.D.).; orcid.org/0000-0002-8861-8619; Email: deplano@unica.it

Andrea Cannizzo − *Institute of Applied Physics, University of Bern, Bern CH-3012, Switzerland;* orcid.org/0000-0002-2325-0112; Email: andrea.cannizzo@unibe.ch

Authors

Michela Gazzetto − *Institute of Applied Physics, University of Bern, Bern CH-3012, Switzerland;* orcid.org/0000-0002-1968-7258

Flavia Artizzu − *Department of Sustainable Development and Ecological Transition (DISSTE), University of Eastern Piedmont, Vercelli I-13100, Italy;* orcid.org/0000-0003-3773-2806

Salahuddin. S. Attar − *Dipartimento di Scienze Chimiche e Geologiche, Università di Cagliari, Cagliari I-09042, Italy;* Present Address: College of Science and Engineering Hamad Bin Khalifa University, Education City, Doha 34110, Qatar (S.S.A.); orcid.org/0000-0003-1341-2218

Jakob T. Casanova − *Institute of Applied Physics, University of Bern, Bern CH-3012, Switzerland*

Luciano Marchiò − *Dipartimento di Scienze Chimiche, della Vita e della Sostenibilità Ambientale, Università di Parma, Parma I-43124, Italy;* orcid.org/0000-0002-0025-1104

Luca Pilia − *Dipartimento di Ingegneria Meccanica, Chimica e dei Materiali, Università di Cagliari, Cagliari I-09123, Italy;* orcid.org/0000-0001-8753-7094

Antonio Monari − *ITODYS, Université Paris Cité and CNRS, Paris F-75006, France;* orcid.org/0000-0001-9464-1463

Complete contact information is available at: https://pubs.acs.org/10.1021/jacs.6c00565

Notes

The authors declare no competing financial interest.

■ ACKNOWLEDGMENTS

M.C., J.T.C., and A.C. thank the Swiss National Science Foundation (grant 200021_212891). L.P., F.A., and A.C. were supported by the European Innovation Council (project "ARTEMIS" G.A. 101115149). F.A. and L.P. thank the Italian Ministry of University and Research and European Union (PRIN PNRR: P2022PKW4T). P.D., S.S.A., and L.P. acknowledge the Università degli Studi di Cagliari (Italy).

■ REFERENCES

(1) (a) Viswanath, G.; Kasha, M. Confirmation of the Anomalous Fluorescence of Azulene. *J. Chem. Phys.* **1956**, *24* (3), 574−577. (b) Itoh, T. Fluorescence and Phosphorescence from Higher Excited States of Organic Molecules. *Chem. Rev.* **2012**, *112* (8), 4541−4568.

(2) Demchenko, A. P.; Tomin, V. I.; Chou, P. T. Breaking the Kasha Rule for More Efficient Photochemistry. *Chem. Rev.* **2017**, *117* (21), 13353−13381.

(3) (a) Chang, Y. C.; Tang, K. C.; Pan, H. A.; Liu, S. H.; Koshevoy, I. O.; Karttunen, A. J.; Hung, W. Y.; Cheng, M. H.; Chou, P. T. Harnessing Fluorescence versus Phosphorescence Branching Ratio in (Phenyl)(n)-Bridged (n = 0−5) Bimetallic Au(I) Complexes. *J. Phys. Chem. C* **2013**, *117* (19), 9623−9632. (b) Yeow, E. K. L.; Steer, R. P.

Energy transfer involving higher electronic states: a new direction for molecular logic gates. *Chem. Phys. Lett.* **2003**, *377* (3−4), 391−398.

(4) Shi, L.; Yan, C.; Guo, Z.; Chi, W.; Wei, J.; Liu, W.; Liu, X.; Tian, H.; Zhu, W. H. De novo strategy with engineering anti-Kasha/Kasha fluorophores enables reliable ratiometric quantification of biomolecules. *Nat. Commun.* **2020**, *11* (1), 793.

(5) (a) Myahkostupov, M.; Pagba, C. V.; Gundlach, L.; Piotrowiak, P. Vibrational State Dependence of Interfacial Electron Transfer: Hot Electron Injection from the S$_1$ State of Azulene into TiO$_2$ Nanoparticles. *J. Phys. Chem. C* **2013**, *117* (40), 20485−20493. (b) Becker, R. S.; Pelliccioli, A. P.; Romani, A.; Favaro, G. Vibronic Quantum Effects in Fluorescence and Photochemistry. Competition between Vibrational Relaxation and Photochemistry and Consequences for Photochemical Control. *J. Am. Chem. Soc.* **1999**, *121* (10), 2104−2109.

(6) (a) Nazari, M.; Bosch, C. D.; Rondi, A.; Frances-Monerris, A.; Marazzi, M.; Lognon, E.; Gazzetto, M.; Langenegger, S. M.; Haner, R.; Feurer, T.; et al. Ultrafast dynamics in polycyclic aromatic hydrocarbons: the key case of conical intersections at higher excited states and their role in the photophysics of phenanthrene monomer. *Phys. Chem. Chem. Phys.* **2019**, *21* (31), 16981−16988. (b) Röhrs, M.; Escudero, D. Multiple Anti-Kasha Emissions in Transition-Metal Complexes. *J. Phys. Chem. Lett.* **2019**, *10* (19), 5798−5804. (c) Franz, J.; Oelschlegel, M.; Zobel, J. P.; Hua, S. A.; Borter, J. H.; Schmid, L.; Morselli, G.; Wenger, O. S.; Schwarzer, D.; Meyer, F.; et al. Bifurcation of Excited-State Population Leads to Anti-Kasha Luminescence in a Disulfide-Decorated Organometallic Rhenium Photosensitizer. *J. Am. Chem. Soc.* **2024**, *146*, 11272−11288.

(7) Maafi, M. Excitation Wavelength-Dependent Photochemistry. *Photochem* **2024**, *4* (2), 233−270.

(8) Attar, S.; Espa, D.; Artizzu, F.; Mercuri, M. L.; Serpe, A.; Sessini, E.; Concas, G.; Congiu, F.; Marchio, L.; Deplano, P. A Platinum-Dithiolene Monoanionic Salt Exhibiting Multiproperties, Including Room-Temperature Proton-Dependent Solution Luminescence. *Inorg. Chem.* **2016**, *55* (11), 5118−5126.

(9) Attar, S.; Espa, D.; Artizzu, F.; Pilia, L.; Serpe, A.; Pizzotti, M.; Di Carlo, G.; Marchio, L.; Deplano, P. Optically Multiresponsive Heteroleptic Platinum Dithiolene Complex with Proton-Switchable Properties. *Inorg. Chem.* **2017**, *56* (12), 6763−6767.

(10) Attar, S. S.; Artizzu, F.; Marchio, L.; Espa, D.; Pilia, L.; Casula, M. F.; Serpe, A.; Pizzotti, M.; Orbelli-Biroli, A.; Deplano, P. Uncommon Optical Properties and Silver-Responsive Turn-Off/On Luminescence in a Pt(II) Heteroleptic Dithiolene Complex. *Chem. Eur. J.* **2018**, *24*, 10503−10512.

(11) Gazzetto, M.; Artizzu, F.; Attar, S. S.; Marchio, L.; Pilia, L.; Rohwer, E. J.; Feurer, T.; Deplano, P.; Cannizzo, A. Anti-Kasha Conformational Photoisomerization of a Heteroleptic Dithiolene Metal Complex Revealed by Ultrafast Spectroscopy. *J. Phys. Chem. A* **2020**, *124* (51), 10687−10693.

(12) Gazzetto, M. Ultrafast functional dynamics in carbon nanomaterials and metal complexes, PhD Thesis; University of Bern, 2019..

(13) McNaught, A. D.; Wilkinson, A. *Compendium of Chemical Terminology*; Blackwell Science, 1997.

(14) Ielo, I.; Lanza, S.; Campagna, S.; Giannetto, A. The Reversible Formation of Tight Ion Pairs within Platinum(II) Complexes – A Study of Thermodynamic Parameters Governing Noncovalent Interactions. *Eur. J. Inorg. Chem.* **2016**, *2016* (2), 281−287.

(15) Giannetto, A.; Nastasi, F.; Puntoriero, F.; Bella, G.; Campagna, S.; Lanza, S. Fast transport of HCl across a hydrophobic layer over macroscopic distances by using a Pt(ii) compound as the transporter: micro- and nanometric aggregates as effective transporters. *Dalton Trans.* **2021**, *50* (4), 1422−1433.

(16) Frei, F.; Rondi, A.; Espa, D.; Mercuri, M. L.; Pilia, L.; Serpe, A.; Odeh, A.; Van Mourik, F.; Chergui, M.; Feurer, T.; et al. Ultrafast electronic and vibrational relaxations in mixed-ligand dithione-dithiolato Ni, Pd, and Pt complexes. *Dalton Trans.* **2014**, *43* (47), 17666−17676.

(17) Nazari Haghighi Pashaki, M.; Mosimann-Schönbächler, N.; Riede, A.; Gazzetto, M.; Rondi, A.; Cannizzo, A. Two-dimensional ultrafast transient absorption spectrograph covering deep-ultraviolet to visible spectral region optimized for biomolecules. *JPhys Photonics* **2021**, *3* (3), 034014.

Supplementary information

Beyond-Kasha Photochemistry in a heteroleptic platinum-dithiolene complex

Michela Gazzetto,[1] Flavia Artizzu,[2] Salahuddin. S. Attar,[3] Jakob T. Casanova,[1] Luciano Marchiò,[4] Luca Pilia,[5] Antonio Monari,[6] Paola Deplano,[3*] Andrea Cannizzo[1*]

[1] Institute of Applied Physics, University of Bern, CH-3012 Bern, Switzerland. [2] Department of Sustainable Development and Ecological Transition (DISSTE), University of Eastern Piedmont, I-13100 Vercelli, Italy. [3] Dipartimento di Scienze Chimiche e Geologiche, Università di Cagliari, I-09042 Monserrato (CA), Italy. [4] Dipartimento di Scienze Chimiche, della Vita e della Sostenibilità Ambientale, Università di Parma, I-43124 Parma, Italy. [5] Dipartimento di Ingegneria Meccanica, Chimica e dei Materiali, Università di Cagliari, I-09123 Cagliari, Italy. [6] Université Paris Cité and CNRS, ITODYS, F-75006, Paris, France. [7]

*corresponding authors: andrea.cannizzo@unibe.ch, deplano@unica.it.

SI.1 Transient Absorption set-up

The 800 nm pump pulse was generated by 1 KHz Ti:Sapphire regenerative amplifier (Coherent Elite Duo Femto). Energy per pulse was 100 nJ at the sample position and was focused into a ca. 60 µm diameter spot size (1/e^2). The 400 nm pump pulse was obtained frequency doubling with a thin 0,25 mm BBO the 800 nm pump pulse. Energy per pulse was 65 nJ at the sample position with a focus of c.ca 60 µm. The probe pulse was a broadband continuum, generated by focusing a fraction of the Ti:Sapphire fundamental into a 5 mm thick CaF_2 crystal. The relative delay between pump and probe was delayed by a computer-controlled delay stage (Nanotec Electronic with PS 35 controller stage by OWIS GmbH) in the pump beamline. A referenced detection scheme was adopted: the continuum pulse was split by a 50/50 beam splitter into two beams, which were then focused into two different spots of the sample with ca. 40 µm diameter spot size. Only one of the two spots was overlapped with the pump pulse, while the other was kept unperturbed for referencing (in the following probe and reference, respectively). After the sample both probe and reference are collimated by an achromatic doublet lens, dispersed by a grating and then focused into two fast CMOS cameras capable of measuring individual shots (Glaz PulseSync, Synertronic Designs). Spectral- and amplitude fluctuations of the continuum were then corrected shot-per-shot by dividing the probe spectrum by the reference one. A reference baseline for pump-reference ratio was recorded for each measurement by introducing a mechanical chopper in the pump beamline at 0.5 kHz to block every alternate pump pulse. A photo-diode after the chopper was used to monitor shot to shot pulse intensity in order to sort out 'pumped' and 'unpumped' measurements and to compensate for fluctuations and drifts of the pump pulse intensity. All these corrections were applied to single-shot TA signals ($TA_i(t,\lambda)$) before averaging over 2000 shots for each pump-probe time delay:

$$TA(t,\lambda) = \frac{1}{ln(10)}\left[1 - \frac{p_0}{p}\left(\frac{I_{s,1}(t,\lambda)}{I_{r,1}(t,\lambda)}\right) \div \left(\frac{I_{s,0}(t,\lambda)}{I_{r,0}(t,\lambda)}\right)\right]$$

with $I(t,\lambda)$ the spectrum recorded by the camera averaged on 2000 shots. The index s and r refer to the spectra recorded by the camera monitoring the probe and reference pulses, respectively. The index 1 and 0 refer to whether the indexed spectrum was pumped or unpumped respectively. The sorting criterion as stated before, is provided by a photo-diode. The normalization is accounted for by p_i which is the pump intensity recorded by the second photo-diode that is also indexed in the same fashion; since p_0 is a reference value of pump intensity collected at the very beginning of the scan the fraction p_0/p_i takes into account both the shot-to-shot fluctuations and the slow drifts of the laser intensity.

The signal was then calculated accordingly to the following equation,

$$TA(t,\lambda) = \frac{1}{n}\sum_{i=1}^{n} TA_i(t,\lambda)$$

A power dependence measurement was regularly carried out to ensure that experiments are conducted in the linear absorption regime.

SI.2 Steady state and ns time resolved optical measurements and effects of HCl addition

Upon adding HCl, the color of the solution of [Pt((*R*)-α-MBAdto)(quinoxdt)]$^{-}$ complex in acetonitrile changes from deep blue to green (Figure S1A). A substantial change in the absorption is observed as shown in Figure S1A. The lowest absorption band at 600 nm disappears, while a new one is formed around 800 nm. The process varies with addition of HCl aliquots and it is complete for a 1:1 molar ratio between HCl and the complex. As reported in the main text, this is due to the formation of a tight adduct between HCl and the dithioxamidato ligand (MBAdto), where N··H··Cl interaction stabilizes the ion-pair. The formation of tight-contact ion-pairs between N,N′-dialkyldithiooxamidate Pt-Pd metal complexes with HCl has been extensively investigated by Lanza, Campagna and coworkers.[18] Further support on the nature of these tight-contact pairs has been provided by a structural characterization of a related Rh complex, ([(C$_5$Me$_5$)ClRh(H$_2$-isopropyl$_2$DTO k-S,S Rh)]$^+$Cl$^-$)·CHCl$_3$,[19] showing that the two amidic N-H moieties of the coordinated dithiooxamide act as hydrogen bond donor groups towards a chloride ion. The obtained values of bond lengths, bond angles and directionality of the ionic hydrogen-bonding (IHB) compared with literature data[20 21] can explain the formation of associated tight ion-pair that only polar solvents with donor atoms such as Me$_2$SO, MeOH are able to remove HCl from tight ion-pair.[18, 19-21] Our results are fully consistent with these findings and are supported by computational studies. The calculated absorption spectrum, indeed, nicely matches the experimental one (Figure S1 and Table S1). The emission colour changes from 720 nm to 570 nm with a higher emission quantum yield (Φ) of 1.4x10^{-4}. The excitation spectrum at $\lambda_{emission}$=570 nm is peaked at around 410 nm after HCl addition. Also in this case no photoluminescence is observed upon excitation of the lowest absorption band, pointing to a non-Kasha emission behavior.

Time-resolved emission measurements in acetonitrile solution in the presence of HCl reveal a biexponential decay dynamics (Figure S2A and Table S2) in the ns range.

The sequence of frontier molecular orbitals (MOs) in the presence of HCl (Figure S1C) does not change and it is still confirmed the charge-transfer character of the transitions. Indeed, the HOMO → LUMO transition (HOMO = highest occupied molecular orbital; LUMO = lowest unoccupied molecular orbital), which corresponds to the ground state → S$_1$, is still a ligand-to-ligand charge transfer to MBAdto moiety. This transition is stabilized from the presence of HCl and peaked at around 800 nm, with the central Pt more involved in the molecular orbitals respect to the case of **1**(Figure S1A). The ground state → S$_2$ transition is namely a HOMO-1 → LUMO with a very small oscillator strength. The next strongly allowed transition is the ground state → S$_3$, which is a HOMO → LUMO+1 transition with a (mixed metal) intra-ligand charge transfer character to the quinoxdt moiety.

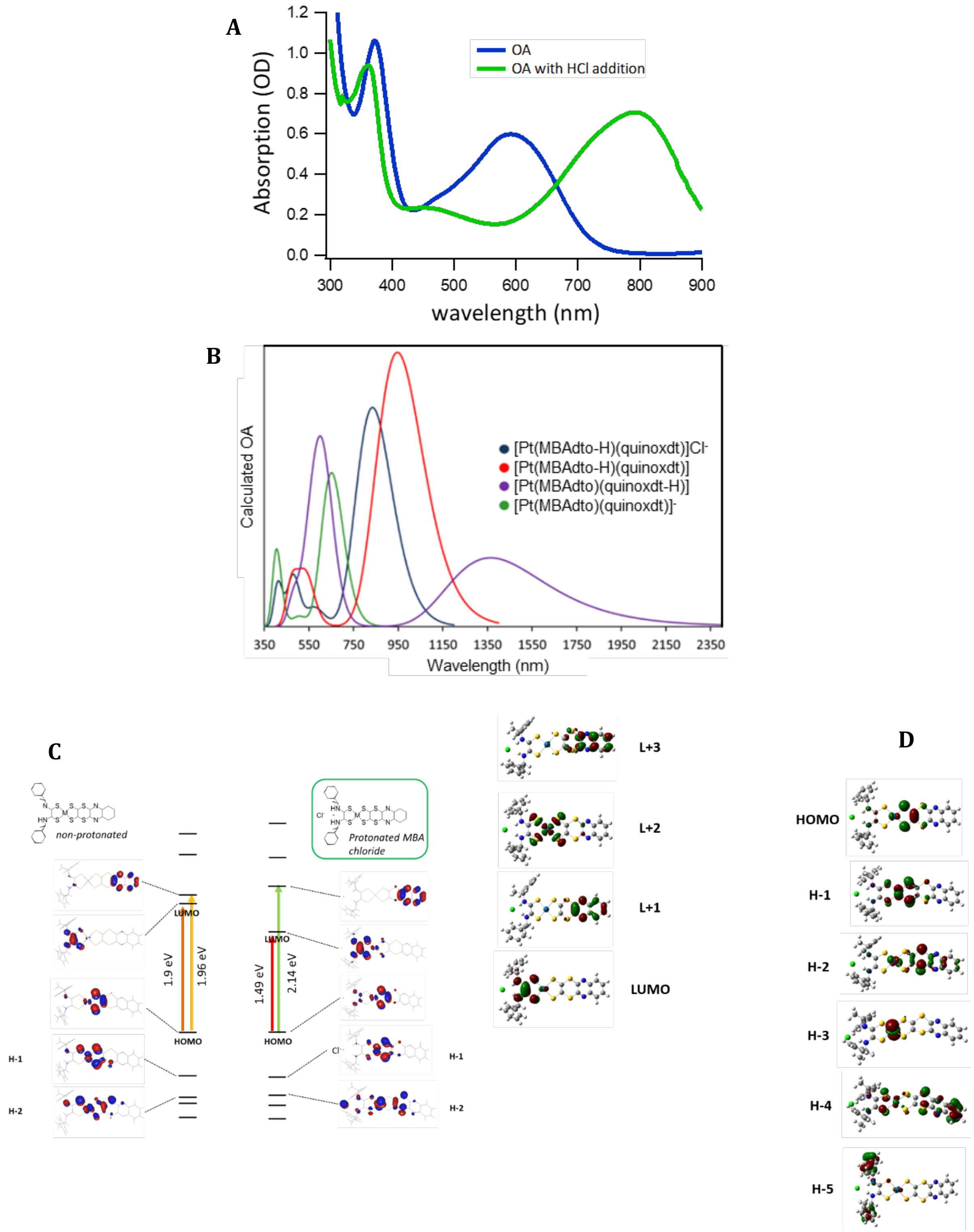

Figure S1: A) UV-Vis optical absorption (OA) spectra of $^-$complex **1** with and without HCl addition. B) Simulated UV-vis spectra for the first ten singlet to singlet transitions of [Pt(MBAdto-H)(quinoxdt)]Cl$^-$ or **1·HCl** (blue line), [Pt(MBAdto-H)(quinoxdt)] (red line), [Pt(MBAdto)(quinoxdt-H)] (purple line), [Pt(MBAdto)(quinoxdt)]$^-$ (green line). C) Comparison of energies of the calculated molecular orbitals (MOs) of 1 and **1·HCl** in solution. D) DFT calculated MOs of **1·HCl** $^-$ in acetonitrile. Molecular orbitals and structures adapted from ref. 9, copyright 2017 American Chemical Society.

Other strongly allowed higher excited state transitions are HOMO-2 → LUMO and HOMO-5 → LUMO, which are centered in the spectral region where is found the excitation band of the non-Kasha emission is found. The first one is a MMLCT, with transfer of charge density from mixed Pt-quinoxdt molecular orbital to the MBA moiety, while the second one is an intra-ligand transition localized on the MBAdto moiety, where the tight contact-pair is located.

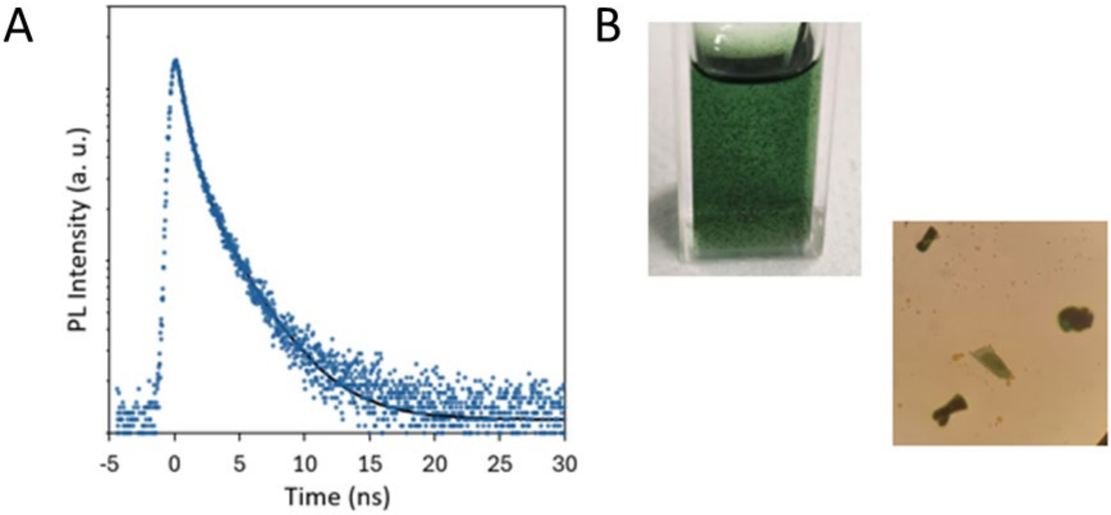

Figure S2: a) Time-resolved emission decay curve of **1·HCl** (blue dots). The solid black line represents the best fit to data for a biexponential decay (Table S2). λ_{exc} = 375 nm, λ_{em} = 560 nm; b) Photographs of the aggregate particles formed after irradiation. The optical microscope image shows that the particles are constituted by green crystals.

To investigate the non-Kasha behaviour of the complex we carried on fs TA experiment in HCl solution with ratio 1:3 [**1**]:[HCl]. At first we have excited the lowest transition to S_1 upon 800 nm excitation, than we performed the experiments upon 400 nm excitation, corresponding to excitation of the non-Kasha emission.

Table S1: TD-DFT calculated energies and compositions of the lowest lying singlet electronic transitions **1·HCl** $^-$ in the solution phase, acetonitrile, (B3LYP/6-31+G(d)-SDD). The principal singlet transitions responsible for the main absorption band in the visible-NIR region are shown in bold, while the ones mainly responsible of the non-Kasha emission are underlined.

State	**Composition**[a]	**ΔE(eV/nm)**[b]	**f** [c]	**Character**
1	**HOMO → LUMO, 100%**	**1.49 / 835**	**0.2304**	quinoxdt /Pt → MBAdto/Pt
2	HOMO-1 → LUMO, 98%	1.97 / 630	0.0008	
3	**HOMO → LUMO+1, 99%**	**2.14 / 578**	**0.0175**	quinoxdt /Pt → quinoxdt
4	HOMO → LUMO+2, 97%	2.20 / 558	0.0019	
5	HOMO-3 → LUMO, 89%	2.27 / 547	0.0005	
6	HOMO-2 → LUMO, 88%	2.58 / 481	0.0541	quinoxdt /Pt → MBAdto /Pt
7	HOMO-1→ LUMO+2, 94%	2.83 / 438	0.0003	
8	HOMO-4 → LUMO, 66% HOMO-12 → LUMO, 20%	2.91 / 426	0.0024	
9	HOMO-5 → LUMO, 83%	3.01 / 412	0.0454	MBAdto → MBAdto/Pt

Table S2. Time-resolved PL data for **1·HCl**.

τ_n (ns)	**Contribution (%)** [a]	**τ_{av} (ns)**[a]
0.777(8)	39	2.20
3.13(5)	61	

[a] Intensity average lifetime calculated as $\tau_{av} = \frac{\sum a_i \tau_i^2}{\sum a_i \tau_i}$

SI.3 Investigation of the photocycle upon 800 nm excitation

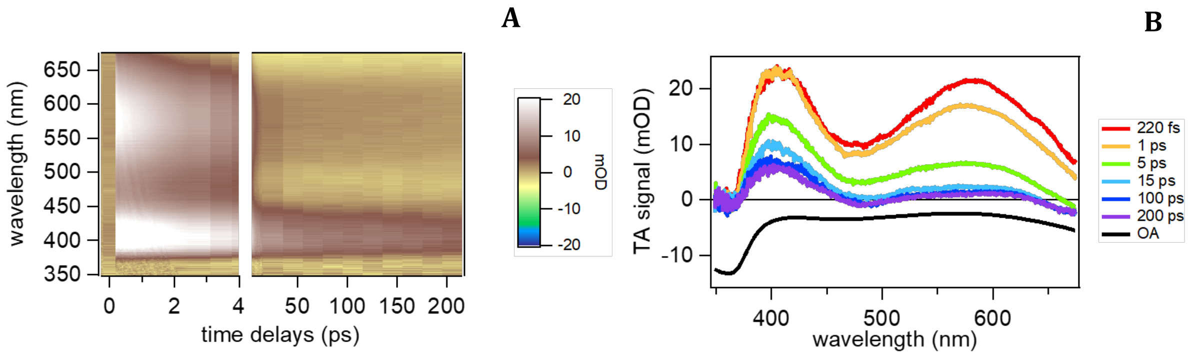

Figure S3: A) fs TA time-wavelength plot of **1·HCl** upon 800 nm excitation in acetonitrile. B) Spectra at selected time delays from panel A). The steady-state absorption spectra are reported inverted to match the TA spectra and to help the assignment of the transitions.

Figure S3A reports the fs TA experiment upon 800 nm excitation and Figure S3B shows the spectra at selected time delays. Two strong ESA bands develop within the instrumental time resolution, peaked at 410 nm and 580 nm, respectively. The negative bands centered at 360 nm, 480 nm and in the low energy region (λ_{probe} > 650 nm) closely match the inverted absorption spectrum and are therefore attributed to GSB. It has to be noted that in this situation we cannot distinguish if the ESA bands are effectively one or more. It could be that we are observing one sole broad ESA band peaked at 480 nm, overlapping with GSB also peaked at 480 nm, as well as we are observing two or more ESA bands. Before any analysis we can observe that the excited state lifetime must be in the ns range, confirming what was expected in literature from steady state analysis.

By means of SVD data analysis, TA were spectrally decomposed into four DAS, shown in Figure S4, each decaying with its own lifetime: 0.9 ps, 3.9 ps, 120 ps and ∞. DAS τ_1= 0.9 ps describes an ESA energy redistribution, with a decay of the ESA peak at 580 nm and a growth of the one at 410 nm. If we make the hypothesis that we are observing just one ESA band, DAS τ_1 describes a blue shift of the ESA. Considering the timescale, this mechanism can be safely attributed in both cases to vibrational cooling in the S_1 state. DAS τ_2= 3.9 ps describes an overall decay of the whole signal, with a stronger decay of the ESA at lower energies. Considering the fact that the complex is not emissive and confronting the result with our previous analysis for just the heteroleptic complex, we assign these dynamics to ISC and cooling in the triplet excited state. DAS τ_3= 120 ps describes a decay of the overall signal without any change in the spectral pattern. Both the 100s of ps time scale and the spectral evolution is typical of rotational diffusion. Accordingly, we can safely assign this DAS to such a process. DAS τ_4 is modelled with a step function and describes ground state recovery with a contribution to the dynamics much longer than the scanned interval, pointing to excited state lifetime in the ns range as previously observed.

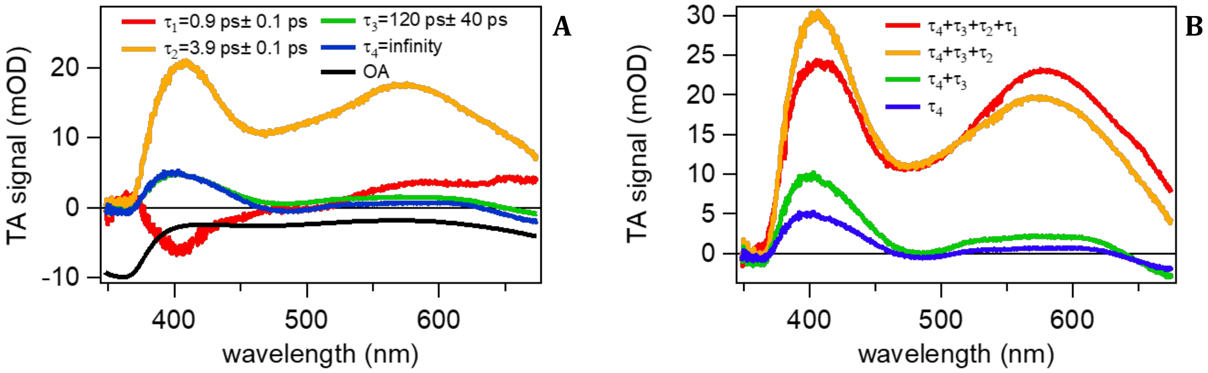

Figure S4: A) DAS obtained by SVD analysis of fs TA experiment upon 800 nm excitation. Each curve is labelled with the respective time constant. τ_4 describes a contribution with dynamics much longer than the scanned interval and is modelled with a step function. B) DAS sums reconstructing the experimental dynamics.

This is substantially identical to what found with complex **1** upon excitation within the lowest absorption (615 nm)[11]. The only difference is the spectral shape between 500 nm and 650 nm and can be explained as a shift of the GSB from 610 nm to 680 nm. The study on the **1·HCl** at 800 nm shows that the presence of the HCl has no effect on the excited state and its dynamics.

SI.4 Comparison of the earlier transient absorption signal upon 800 nm and 400 nm excitations

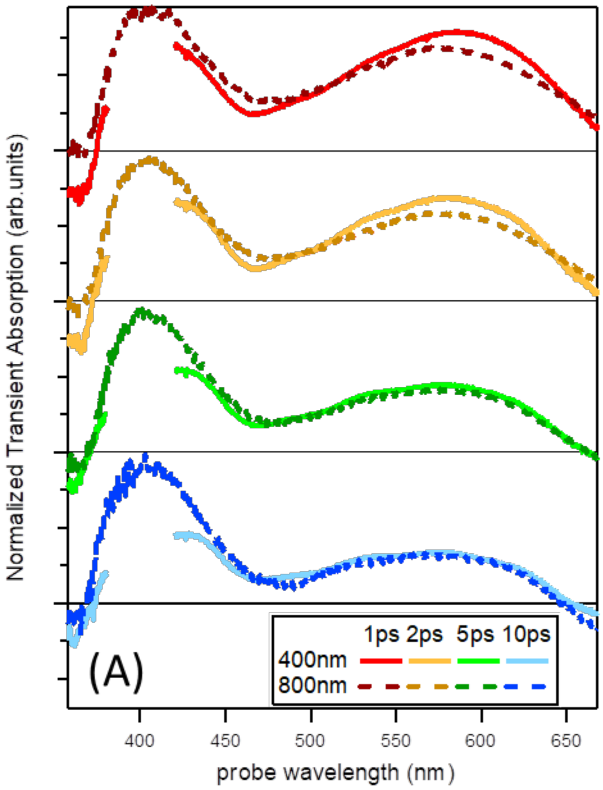

Figure S5. Comparison of TA spectra representative of the spectral evolution in the range 1 to 10 ps, namely after all the internal conversion processes and before of the delayed emission. For sake of comparison spectra are vertically shifted and normalized to match in the region 500-650 nm. Horizontal black lines are the respective zero lines.

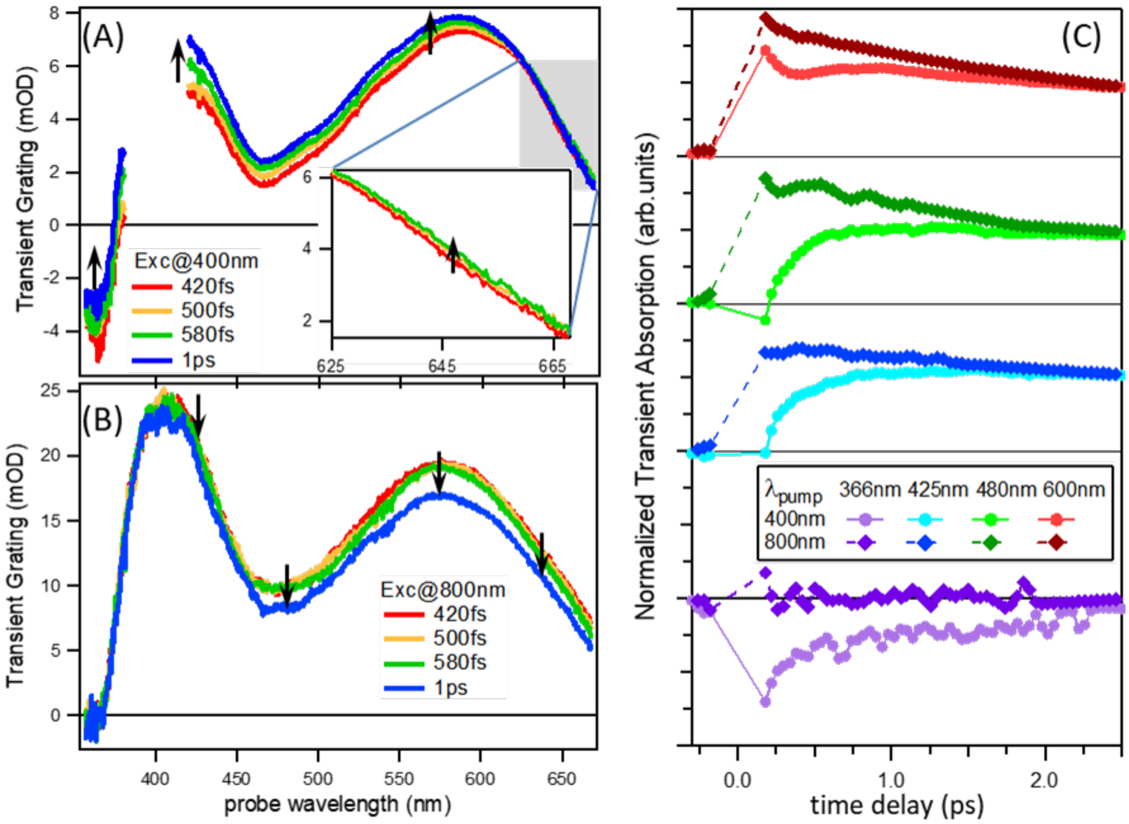

Figure S6. Comparison of representative TA spectra upon excitation at 400 nm (A) and 800 nm (B) to show the sub-ps rise (decay) of the signal upon 400 nm (800 nm) excitation, as highlighted by the black arrows. Inset in panel (A) zooms in the range at λ>625 nm to show that the rise upon 400 nm excitation is ubiquitous. The presence of the rise only upon 400 nm excitation is clearly observed by comparing kinetic traces at selected wavelengths. For the sake of comparison, kinetic traces are normalized to overlap in the ps timescale.

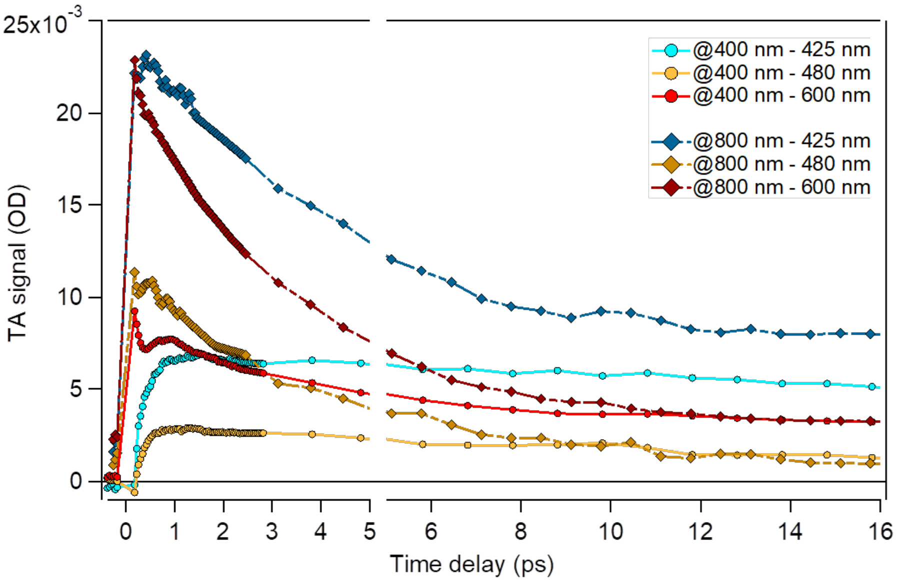

Figure S7. Comparison of representative TA kinetic traces upon excitation at 400 nm and 800 nm on a fresh sample.

SI.5 Comparison of the TA signals of the fresh sample upon 800 nm excitation and of a photo-exposed sample upon 400 nm excitation

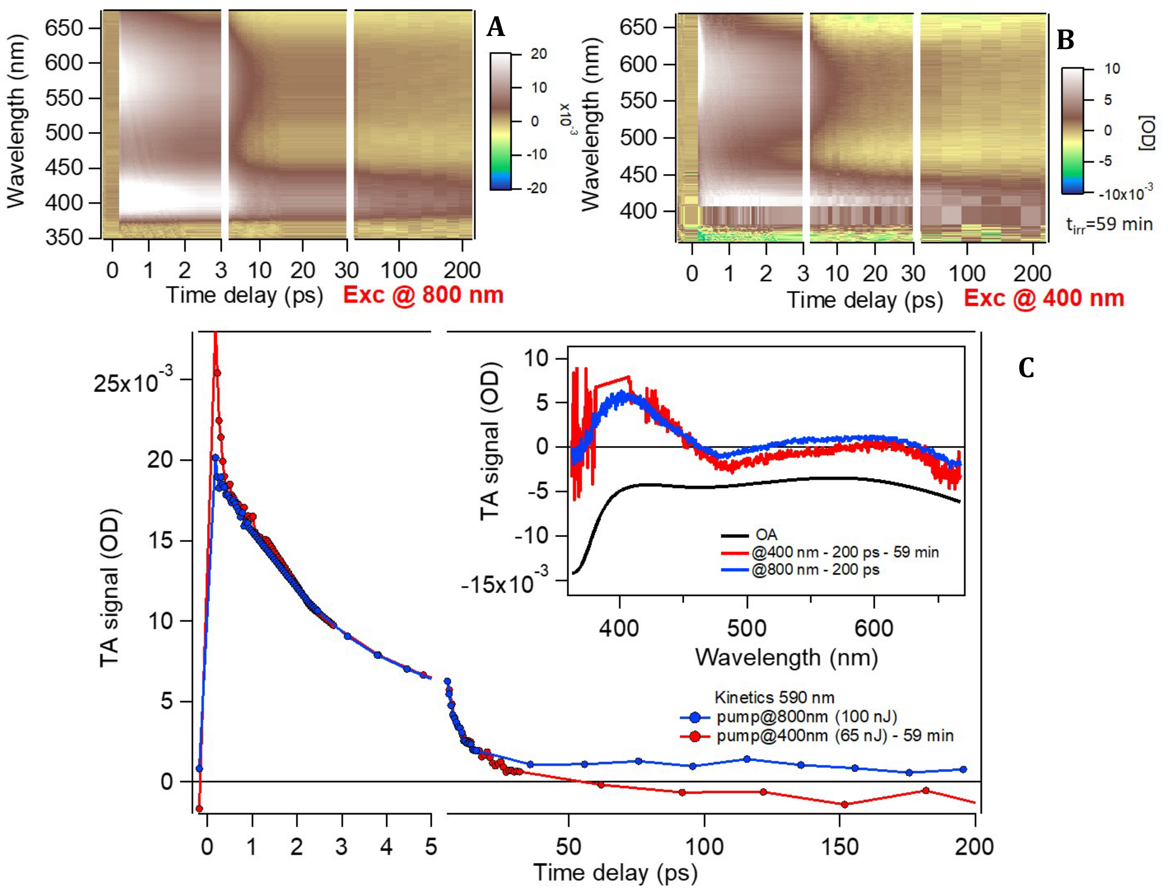

Figure S8. 2D TA signals (A) upon 800 nm excitation on a fresh sample and (B) upon 400 nm on a sample after 59min of irradiation, which corresponds to a completed SE quenching dynamics (see Figure 4 and Figure S9). (C) Kinetic traces at 590 nm and (inset) the spectra at 200 ps extracted from the two 2D plots. The two data sets are essentially the same except in the earlies, sub-ps, time range and at the latest times, where the irradiated sample still shows a very small negative signal, revealing a very small emission signal.

SI.6 Fitting of the quenching kinetics with the Avrami equation.

According to the Avrami equation (eq. 1) and eq. 2, we fitted data in in panel B of Figure 4 and Figure S9 with the function:

$$TA_{SE}(t_{irr}) - TA_{SE}(\infty) = \left(TA_{SE}(\infty) - TA_{SE}(0)\right) \cdot \left[1 - e^{-Kt^4}\right] = -\Delta \cdot e^{-Kt^4} + TA_{SE}(\infty) \qquad \text{eq. S1}$$

where we replaced t_{ncl} with t_{irr} and, for sake of readability, TA_{590nm}^{220ps} with TA_{SE}. The fitting coefficients are reported in Table S3.

λ_{Pm} (nm)	550	580	605	$\langle 580-600 \rangle$ (from Figure 4B)
Δ (mOD)	(4.9 ± 0.5) 10^{-3}	(3.2 ± 0.5) 10^{-3}	(2.5 ± 0.5) 10^{-3}	(2.8 ± 0.3) 10^{-3}
$TA_{SE}(\infty)$ (mOD)	(0.3 ± 0.4) 10^{-3}	(0.2 ± 0.3) 10^{-3}	(0.5 ± 0.3) 10^{-3}	(0.1 ± 0.2) 10^{-3}
K (s^{-4})	(1.9±1.2) 10^{-14} (Global parameter)			(2.5±0.8) 10^{-14}

Table S3 Fitting parameters by interpolation of data in Figure 4B (last column) and Figure S9 with eq. S1. Data in Figure 4B are obtained averaging over the range 580 to 600nm.

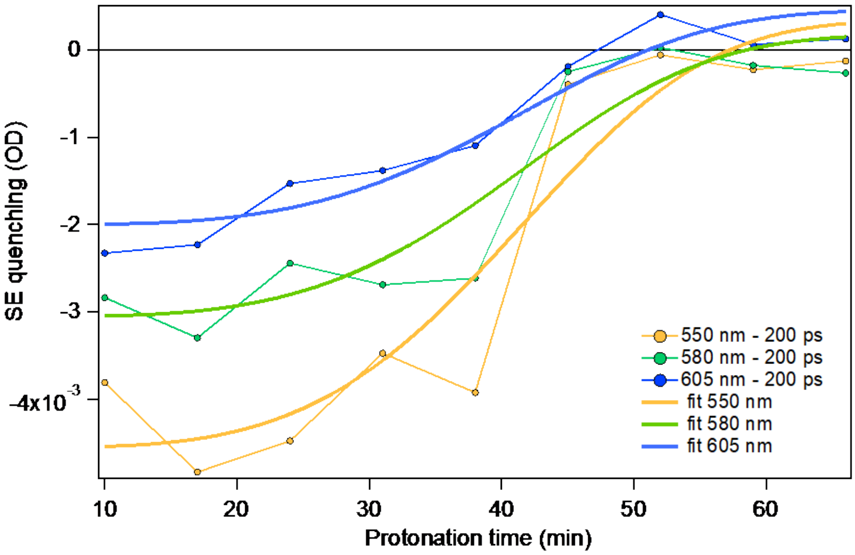

Figure S9. SE quenching kinetics monitored as the amplitude of TA signal at 220 ps (the longest scanned delay time) at different probe wavelengths. The solid line is obtained by fitting the data to eq. 1

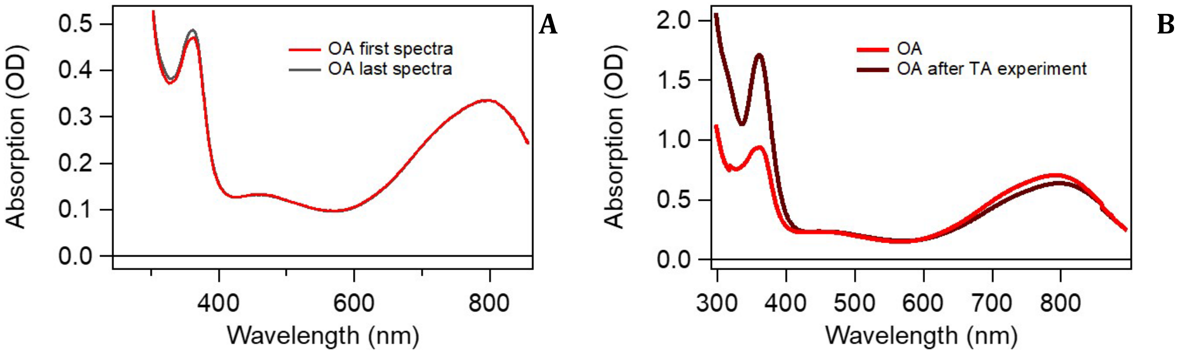

Figure S10. A) First (red) and last (black) steady state electronic absorption spectra measured with the sample kept in the spectrophotometer (mainly in the dark without exposition to the 400nm laser pump) in 2 hours of scans every 4 minutes. B) Steady state electronic absorption spectra before (red) and after (brown) the experiment. The increase of the signal at shorter wavelengths is tentatively assigned to the aggregate formation.

SI.7 Calculation of the fraction of excited molecules

As reported in the main text the experiment to investigate the photo-accumulation kinetic (Figure 4 and Figure S9) was carried out on 2 mL of solution with concentration c=4.43x10^{-4} M and with pulses of 65nJ energy each. Each scan was 7 min long with an excitation repetition rate of 500 Hz. According to these values the number of molecules in solution (N_{mol}) is

$$N_{mol}=N_A \bullet 4.43\ 10^{-4} \bullet 2\ 10^{-3} = N_A \bullet 9\ 10^{-7} = 6\ 10^{23} \bullet 9\ 10^{-7} = 0.54\ 10^{18},$$

while the total number of photons per pulse ($N_{ph/pulse}$) is

$$N_{ph/pulse} = 65\text{nJ}/h\nu_{400} = 1.3\ 10^{11}\ \text{photons/pulse}.$$

where $h\nu_{400}$ is the energy of a 400 nm photon (=3.1eV or 0.50 10^{-18} J).

Since the concentration was chosen to be roughly 0.3 OD at 400 nm and we took care to work in a linear regime the number of excited molecule per pulse ($N_{Exc\_mol/pulse}$) is equal to the number of absorbed photons:

$$N_{Exc\_mol/pulse} = N_{ph/pulse} \bullet 10^{-OD} = N_{ph/pulse} \bullet 0.5 = 6.5\ 10^{10}$$

and the fraction of excited molecule per pulse (R_{pulse}) which is given by

$$R_{pulse} = N_{Exc\_mol/pulse}/N_{mol} = 6.5/0.54\ 10^{-8} = 1.2\ 10^{-7}.$$

If we do not take care of reabsorption, the fraction of excited molecules after 40 minutes (R_{40min}) at 500 Hz of pump repetition rate is given by $R_{pulse} \bullet 40 \bullet 60 \bullet 500$= 14.4%, as reported in the main text. A more precise calculation should consider multiple excitations and R_{40min} can be calculated with the following formula:

$$R_{40min} = R_{pulse} \sum_{n=0}^{N_{ph}} \left(1 - R_{pulse}\right)^{n} = R_{pulse} \left[\frac{1-\left(1-R_{pulse}\right)^{N_{ph}+1}}{1-\left(1-R_{pulse}\right)} \right] = 13\%$$

where N_{ph} is the total number of pulses after 40 minutes, *i.e.* N_{ph}=40•60•500=1.2 10^6.

SI.8 Preliminary Results from calculations

As proved by the richness and complexity of the result herein reported as well as in ref. [11], a thoughtful and complete investigation with a non-adiabatic approach is mandatory to identify the possible conformers, the relaxation paths from the different excited states and the role of external parameters, as the solvent and the specific acid.

This extensive computational study is ongoing but some preliminary results, relevant to this article, can already be drawn. In particular, as already reported, [11] the different conformers~~,~~ that can be optically and thermally populated, are present also in the ground state. Therefore, we have been carrying out an extensive characterization of the ground state potential energy surface to map its relevant minima. Consistently with this and previous works, we used Gaussian 16[22]~~,~~ with Becke-three-parameters exchange functional, including the Lee-Yang-Parr correlation potential B3LYP [23] and the 6-31+G(d)[24] [25] basis set. For the Pt atom, the SDD[26] effective core potential was utilized. Including the PCM[27] implicit solvent model using acetonitrile as a solvent. Conversely, the values of spin-orbit couplings (SOCs) and non-adiabatic coupling matrix elements (NACMEs), as well potential energy surfaces (PESs) and natural transition orbitals (NTOs) were calculated with the ORCA software package [28] using the B3LYP/G hybrid functional in combination with the def2-SVP basis set[29]. Relativistic effects were treated perturbatively using the zero-order regular approximation (ZORA)[30], with the uncontracted SARC-def2-SVP basis set[31] applied to the platinum atom, unless stated otherwise. In this section the computational states are labeled alphabetically to distinguish them from the experimentally measured states (namely **S_1** and **S_2**)

The geometric scan along the dihedral angle describing the rotation of one of the flexible benzene units in the MBAdto ligand is shown in Figure S11. The α angle is defined as the rotation of the methyl group about the C–N bond. The global minimum is located at approximately 200°, while the lower of the two local minima occurs at 270°. The highest-energy minimum is found at around 70°. Variations of the α angle may be held responsible for driving the conformational changes in the system on longer time scale, leading to more accessible packing and aggregate formation. By comparing the PES of the system with and without HCl, we propose that the ejection event stabilizes the minimum at an α-torsion of 270°, reducing the overall barrier height and favoring its population.

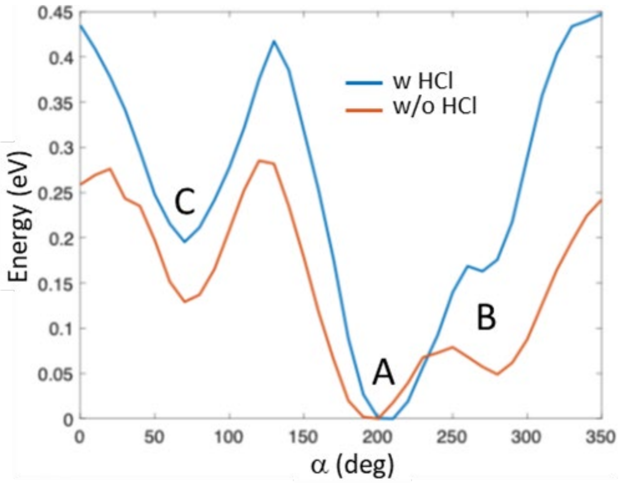

Figure S11. S_0 potential energy, with and without HCl (**1·HCl** and **1**, respectively), as a function of the dihedral angle between one of the methyl group the C–N bond (α-angle in the text). Three minima are observed and in the text are named in order of increasing energy, A, B and C. The used level of theory is[32] ωB97X-D3/def2-SVP.

Not surprisingly, we identified a local minimum which can be thermally populated from the global minimum because it is only 25 meV (40meV when calculated with ORCA) above the global minimum and it is separated by a barrier of 75 meV or less. Therefore, this configuration is the first candidate as the isomer responsible of the precipitate formation. These preliminary results are summarized in Figure S12, where the two configurations are compared. Relevant to this article, we infer from this figure two main results: 1) in the structure of the local minimum the two phen rings are more parallel and ordered, facilitating the formation of packed and ordered aggregates and ultimately of nanoparticles; 2) the local minimum shows an inversion of the electronic spatial distribution with respect to the global minimum, being the former centered on the quinoxdt and the latter on the MBAdto. As discussed in the main text, the latter can explain the observed blue-shift of the emission and the suppression of the ISC.

To estimate the barrier between the two configurations, we used linear morphing between the two structures to track a connecting path and to calculate the energy of the intermediate states. This approach only samples one possible transition, potentially overestimating the barrier, as lower-energy paths may exist.

To better describe the electronic (diabatic) nature of the possible excited-state pathways of interest, we report here the NTOs[33] in Figure S13, for the relevant minima identified in Figure S11. The relevant excited state (corresponding to S_2 in the main text) is named here as $S_{q/p}$ (see Table S4 for labelling). These are characterized by an electron and hole density both localized on the quinoxdt ligand.[11] The NTOs of state of S_1 (here named S_a) are also reported. We observe a substantial independence of the NTOs from the benzene units in the MBAdto ligand.

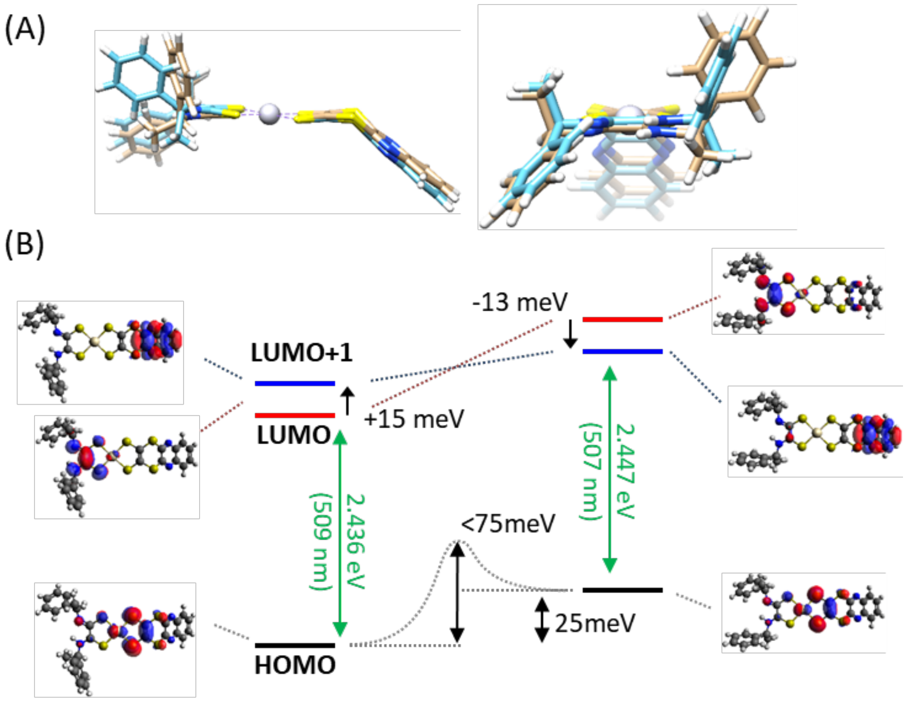

Figure S12. A) a comparison the equilibrium structures of the global and thermally accessible local minima (yellowish and blueish coloured, respectively). B) comparison of the energetics and of the molecular orbitals (only the HOMO and the first two LUMOs are shown) for the global (left) and local minima (right). The calculation are performed in acetonitrile at PCM level.

To estimate the coupling between states, the NACMEs are presented in Table S4 to Table S6. The reported values were calculated for the heteroleptic complex with HCl and represent the NACMEs between the ground state (GS) and the excited states (ES). The NACME values reported in Table S4 are computed for a single, static structure at minimum A. Notably, the coupling associated with **$S_{p/q}$** is relatively high compared to the nearby states. The NACME for the minimum B and C are shown in Table S5 and Table S6, respectively.

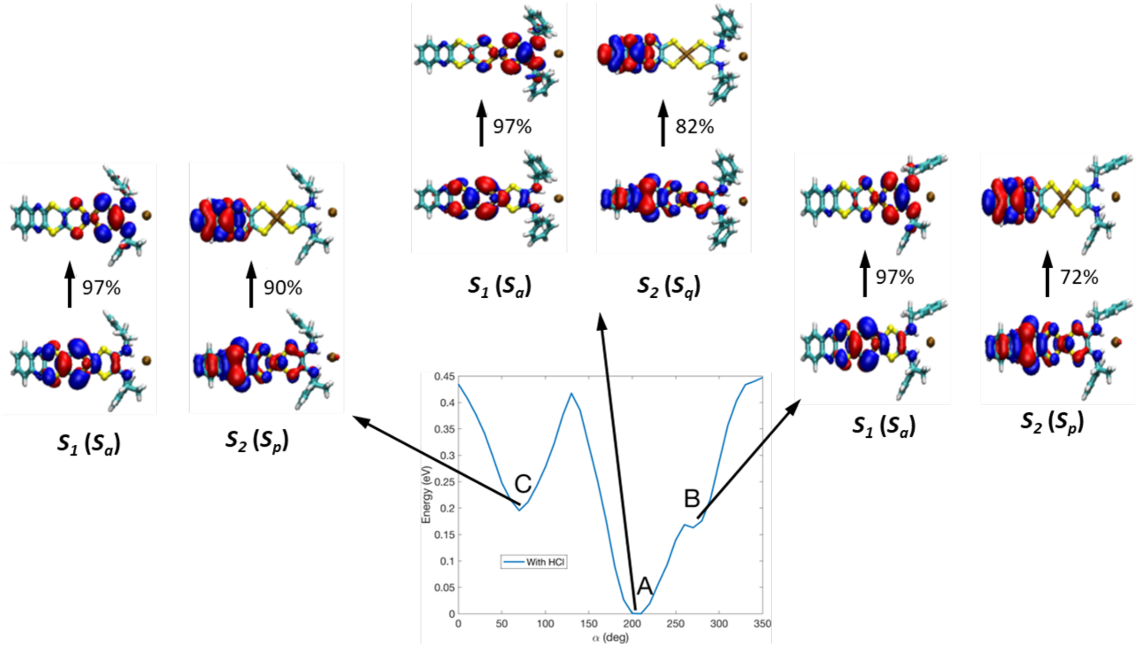

Figure S13: Natural transition orbitals (NTOs) from the ground state (S_0) for the minima of the adduct **1·HCl** shown in Figure S11. The displayed NTOs correspond to the lowest singlet excited state S_a (S_1) and to S_q (S_2), defined as the first higher excited single state with the NTO fully centered on the quinoxdt and with a not-negligible optical oscillator strength.

Table S4: (1st and 3rd columns) Nonadiabatic matrix element (NACMEs) between the ground state (GS) and the relevant singlet and triplet excited states (ES) (2nd and 3rd column, respectively) for the heteroleptic complex with HCl (**1·HCl**). Data calculated for the optimized structure in the minimum A, coupling strength in $\boldsymbol{a}_0^{-1}$.

#	Singlet ES	$\left\lvert\left\langle GS\middle\lvert\frac{d}{dx}\middle\rvert ES\right\rangle\right\rvert$	Triplet ES	$\left\lvert\left\langle GS\middle\lvert\frac{d}{dx}\middle\rvert ES\right\rangle\right\rvert$
1	S_a ($\boldsymbol{S_1}$)	0.97	T_b	1.18
2	S_b	0.31	T_c	1.00
3	S_c	0.56	T_d	0.14
4	S_d	0.23	T_e	0.19
5	S_e	0.24	T_f	0.21
6	S_f	0.36	T_g	0.30
7	S_g	0.089	T_h	0.28
8	S_h	0.16	T_i	0.27
9	S_i	0.18	T_j	0.13
10	S_j	0.20	T_k	0.20
11	S_k	0.24	T_l	0.54
12	S_l	0.16	T_m	0.20
13	S_m	0.24	T_n	0.21
14	S_n	0.19	T_o	0.12
15	S_o	0.21	T_p	0.41
16	S_p ($\boldsymbol{S_2}$)	0.22	T_q	0.13
17	S_q	0.71	T_r	0.18
18	S_r	0.39	T_s	0.19
19			T_t	0.094
20			T_u	0.57
21			T_v	0.59
22			T_w	0.35

Table S5: the same data as in Table S4 but calculated for the optimized structure in the minimum B**.**

#	Singlet ES	$\left|\left\langle GS\middle|\frac{d}{dx}\middle|ES\right\rangle\right|$	Triplet ES	$\left|\left\langle GS\middle|\frac{d}{dx}\middle|ES\right\rangle\right|$
1	S_a ($\boldsymbol{S_1}$)	0.90	T_b	0.15
2	S_b	0.27	T_c	0.97
3	S_c	0.55	T_d	0.34
4	S_d	0.22	T_e	1.1
5	S_e	0.23	T_f	0.19
6	S_f	0.35	T_g	0.18
7	S_g	0.097	T_h	0.33
8	S_h	0.16	T_i	0.35
9	S_i	0.13	T_j	0.62
10	S_j	0.22	T_k	0.40
11	S_k	0.19	T_l	1.0
12	S_l	0.19	T_m	0.052
13	S_m	0.25	T_n	0.36
14	S_n	0.24	T_o	0.25
15	S_o	0.38	T_p	0.63
16	S_p ($\boldsymbol{S_2}$)	0.61	T_q	0.67
17			T_r	0.068
18			T_s	0.26
19			T_t	0.14
20			T_u	0.12

Table S6: the same data as in Table S4 but calculated for the optimized structure in the minimum C.

#	Singlet ES	$\left|\left\langle GS\right|\frac{d}{dx}\left|ES\right\rangle\right|$	Triplet ES	$\left|\left\langle GS\right|\frac{d}{dx}\left|ES\right\rangle\right|$
1	S_a ($\boldsymbol{S_1}$)	0.92	T_b	0.17
2	S_b	0.27	T_c	1.2
3	S_c	0.54	T_d	0.53
4	S_d	0.22	T_e	1.0
5	S_e	0.14	T_f	0.21
6	S_f	0.40	T_g	0.13
7	S_g	0.17	T_h	0.33
8	S_h	0.16	T_i	0.34
9	S_i	0.14	T_j	0.52
10	S_j	0.19	T_k	0.057
11	S_k	0.20	T_l	0.39
12	S_l	0.17	T_m	0.33
13	S_m	0.24	T_n	0.53
14	S_n	0.22	T_o	0.47
15	S_o	0.36	T_p	0.10
16	S_p ($\boldsymbol{S_2}$)	0.68	T_q	0.61
17			T_r	0.37
18			T_s	0.27
19			T_t	0.31
20			T_u	0.36
21			T_v	0.46

The SOC values for minima A, B and C of the acceptor are reported in Table S7, Table S8 and Table S9, respectively. We also calculated the SOC for **1** (data not shown), and we found that, except for a small increase of the average values, the variation and the dependence on the excited states show the same trend.

The experimentally photo-excited state S_q is identified based on the agreement with the excitation wavelength and the oscillator strength. The state T_w corresponds to the triplet state closest in energy to the singlet $\boldsymbol{S_q}$. The SOC between these two states is moderate mostly due to the limited participation of the Pt center to the electronic density reorganization, as discussed in the main text. However, since $\boldsymbol{S_q}$ lies close in energy to $\boldsymbol{T_w}$ (89 cm^{-1}), this energy barrier can be readily overcome, resulting in a high ISC rate. The SOC values in Table S8 between the $\boldsymbol{S_p}$ state and the $\boldsymbol{T_u}$ state are also of moderate magnitude. The same observation applies to the SOC values listed in Table S9 for the corresponding states.

Table S7: Spin-orbit coupling (SOC) between the first six lowest singlet and the closest triplet states and between the photo-excited singlet state (S_q) and the closest triplet state (T_w). The data ware calculated for the optimized static structure of the minimum A. The values are in cm^{-1}.

	T_a	T_b	T_c	T_d	T_e	T_w
S_0	108.2	504.1	19.0	1197.4	100.2	
$S_a\ (\boldsymbol{S_1})$	17.0	400.0	32.2	362.8	38.5	
S_b	36.0	17.5	2.9	79.0	9.0	
S_c	706.6	16.5	15.0	102.7	712.4	
S_d	324.2	70.9	76.8	6.9	43.7	
S_e	1350.8	1843.3	25.3	114.1	1294.9	
$S_q\ (\boldsymbol{S_2})$						36.8

Table S8: Same data as in Table S7 but calculated in the minimum B. T_u indicates the closest triplet state to the photoexcited singlet state S_q. The values are in cm^{-1}.

	T_a	T_b	T_c	T_d	T_e	T_u
S_0	82.6	486.5	23.6	1220.4	165.2	
$S_a\ (\boldsymbol{S_1})$	35.8	439.2	35.0	353.6	99.2	
S_b	36.2	13.8	2.3	85.4	7.1	
S_c	718.0	15.0	11.7	92.5	660.5	
S_d	308.6	42.7	84.9	11.5	43.5	
S_e	1442.3	1842.9	20.7	79.2	1293.9	
$S_p\ (\boldsymbol{S_2})$						45.1

Table S9: Same data as in Table S7 but calculated in the minimum C. T_v indicates the closest triplet state to the photoexcited singlet state Sq. The values are in cm^{-1}.

	T_a	T_b	T_c	T_d	T_e	T_v
S_0	63.5	493.9	22.0	1204.1	171.9	
$S_a(\boldsymbol{S_1})$	39.3	425.9	35.2	365.9	129.2	
S_b	36.8	13.2	2.4	84.0	5.8	
S_c	712.6	32.8	12.7	92.1	665.4	
S_d	318.7	29.0	85.9	7.6	48.6	
S_e	1526.9	1858.3	23.0	47.0	1383.4	
$S_p\ (\boldsymbol{S_2})$						23.3

The SOC values reported in Table S7 to Table S9 allow, along with the corresponding single-triple state energy gap, to estimate roughly the ISC rate between the two states. As written in the main text we observe that the energy gap between $\boldsymbol{S_2}$ ($\boldsymbol{S_{q/p}}$) and the closest triplet state ($\boldsymbol{T_{w/u/v}}$) in the adduct **1·HCl** is almost degenerate (<90cm^{-1}), facilitating ISC. Furthermore, we found that $\boldsymbol{S_2}$ ($\boldsymbol{S_{q/p}}$), which is responsible of the nK response, is very close to several triplet states (typically 2 to 4 triplet states within $\pm k_B T$ at room temperature or $\pm 210\ cm^{-1}$) allowing for a very efficient (sub-100 fs) ISC. Conversely, when we considered the lower excited states, we calculated that in the adduct, regardless the configuration, the $\boldsymbol{T_1}$ is 0.55eV (4700 cm^{-1}) lower than $\boldsymbol{S_1}$, whereas $\boldsymbol{T_2}$ is 0.75eV (6100 cm^{-1}) higher than $\boldsymbol{S_1}$. The relatively small value of the $\boldsymbol{S_1}$-$\boldsymbol{T_1}$ SOC and the important energy gap would suggest a rather long ISC, in agreement with our previous works.[11, 16]

In conclusion of this section, we want to comment on what is maybe the result most relevant to the article, namely that the second excited state ($\boldsymbol{S_b}$) shows systematically lower SOC values regardless of the triplet state. This speaks for a less efficient ISC from this state. Accordingly, to the model presented in the main article, this is the state that becomes the emissive, lowest excited state, after the ejection of the HCl. As can be seen from Figure S1C and D and from Figure S12, in this state, which corresponds to the HOMO→LUMO+1 transition, the excited electron density is completely segregated on the Quinoxdt ligand without any involvement of the Pt orbitals. This condition, which was tentatively identified in the main article as the cause of the dramatic decrease of the ISC rates after the HCl detachment, is now fully confirmed by the calculations.

SI.9 Global fit analysis of the traces from panel A of Figure 4

To quantify the time scales of the different processes responsible of the dynamics shown in Figure 4, we performed a global analysis of the traces in panel A in terms of a multiphasic exponential decay, where the time constants were considered as global variables, meaning the same for all the traces, and the amplitudes as local variables allowed to adapt to the respective curve. The outcome is reported in Figure S14.

All the traces are well described by six exponential decays, whose time constants and amplitudes as a function of HCl addition time are reported in panel B. The time constant of the last component is set to infinity to account for dynamics occurring on time scales much longer than herein investigated time window. It worse noticing that the acquisition time of each trace is 7 minutes (see the main text) and the reported addition time is the time when the scan is concluded. Therefore, the acquisition of the first trace (10min) was started 3 minutes after the HCl addittion and concluded 10 minutes later. As can also be inferred from Figure S14 and Figure S8C), this trace shows on the ps and sub-ps times (the time points first acquired) a signatures typical of **1**, whereas on the 100s ps time scales (the latest acquired spectra) it is much closer to the behaviour of the adducts (see trace at 17min). This means that this trace is due to a dynamical mixture of **1·HCl** and **1** . Accordingly, we should consider the second trace (17 min) more representative of the behaviour of the adducts. More relevant for the sake of this article, we should observe that rise of the stimulated emission is counted mainly by the fifth component of 69 ps, since its amplitude is always opposite in sign with respect to the long-lived component. We exclude that 23 ps, component describes a rise of the SE because. 1) it amplitude has the same sign of the long-lived component; 2) after quenching it does not go to zero, as the fifth one does; 3) the identical behaviour of the kinetics upon 800 nm excitation in this time range (see Figure S8C) proves that this component is not peculiar of the nK process. On the hand, all the components, including the 23 ps one, show a clear change following the quenching, which reveals that the molecules undergo a significant change upon aggregation. The fact that first four components are always present, on the contrary of the fifth and the sixth ones, suggest that they describe processes typical of the complex and not of the HCl dissociation.

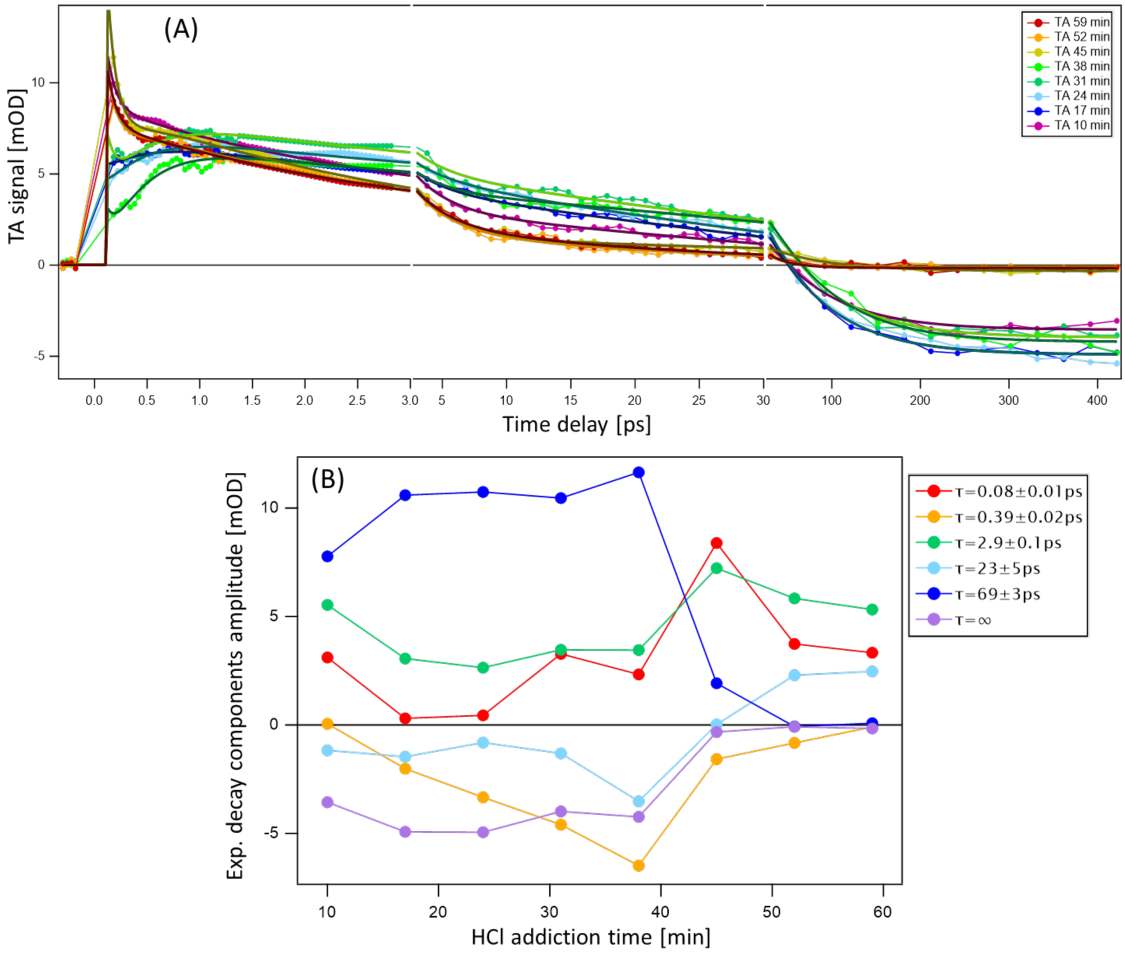

Figure S14. Kinetic traces from Figure 4A analysed with a global fitting approach in terms of 6 exponential decays: Best fitting curves and the parameters (amplitude and time constants) from the global fitting analysis are reported in panel A and B, respectively.

SI.10 Comment on the involvement of triplet states in the non-Kasha emission

As shortly discussed in the main text, we expect that on the tens-of-ps to ns timescale triplet states are populated due to heavy atom effects. This affirmation is also supported by the calculated the spin-orbit coupling reported in section SI.8 (Table S7 to Table S9, and relative discussion). allowing for a possible indirect mechanism of delayed fluorescence, where the emissive state is repopulated from triplet (dark) states.

It is worth bearing in mind that the amplitude of the stimulated emission (SE) is proportional to n, the population of the emissive state during the probe window, multiplied by k, the radiative rate. As discussed in the main text, to have a strong signal comparable to the ground state bealch (GSB), k must correspond to an allowed transition (i.e., 10^8–10^9 s^{-1}), and therefore n must be comparable to the number of excited molecules. Thus, even if the emissive state were populated indirectly, the back-transfer rate from the dark states should be sufficiently high to maintain a population comparable to the total excited-state population. In this regime, the overall lifetime is still determined by the emissive state itself: if its lifetime were only a few picoseconds, the total decay would also occur on the picosecond timescale. Nevertheless, invoking an indirect mechanism could allow for an intermediate scenario, with lifetimes of a few hundred picoseconds and back-transfer on the nanosecond scale. So even if we cannot exclude such a process, we can still conclude that our experimental results speak for an allowed transition with a long lifetime. About the exact nature of the back-transfer, it could be electronic, or it could be the ejection of the HCl itself.

References

(9) Attar, S.; Espa, D.; Artizzu, F.; Pilia, L.; Serpe, A.; Pizzotti, M.; Di Carlo, G.; Marchio, L.; Deplano, P. Optically Multiresponsive Heteroleptic Platinum Dithiolene Complex with Proton-Switchable Properties. *Inorg. Chem.* **2017**, *56* (12), 6763-6767.
(11) Gazzetto, M.; Artizzu, F.; Attar, S. S.; Marchio, L.; Pilia, L.; Rohwer, E. J.; Feurer, T.; Deplano, P.; Cannizzo, A. Anti-Kasha Conformational Photoisomerization of a Heteroleptic Dithiolene Metal Complex Revealed by Ultrafast Spectroscopy. *J. Phys. Chem. A* **2020**, *124* (51), 10687-10693.
(16) Frei, F.; Rondi, A.; Espa, D.; Mercuri, M. L.; Pilia, L.; Serpe, A.; Odeh, A.; Van Mourik, F.; Chergui, M.; Feurer, T.; et al. Ultrafast electronic and vibrational relaxations in mixed-ligand dithione-dithiolato Ni, Pd, and Pt complexes. *Dalton Trans.* **2014**, *43* (47), 17666-17676.
(18) Giannetto, A.; Puntoriero, F.; Barattucci, A.; Lanza, S.; Campagna, S. Tight-Contact Ion Pairs Involving Pt(II) Dithiooxamide Complexes: the Acid−Base Reactions between Hydrohalogenated Ion-Paired Complexes and Pyridine. *Inorg. Chem.* **2009**, *48* (21), 10397-10404. Giannetto, A.; Cordaro, M.; Campagna, S.; Lanza, S. Metal Complexes as Self-Indicating Titrants for Acid–Base Reactions in Chloroform. *Inorg. Chem.* **2018**, *57* (4), 2175-2183.
(19) Askari, B.; Rudbari, H. A.; Valente, A.; Bruno, G.; Micale, N.; Shivalingegowda, N.; Krishnappagowda, L. N. Synthesis, Characterization and Anticancer Studies of Rh(I), Rh(III), Pd(II) and Pt(II) Complexes Bearing A Dithiooxamide Ligand. *Chemistryselect* **2020**, *5* (2), 810-817.
(20) Jeffrey, G. A. *An introduction to hydrogen bonding*; Oxford University Press, 1997.
(21) Steiner, T. The Hydrogen Bond in the Solid State. *Angew. Chem. Int. Ed.* **2002**, *41* (1), 48-76.
(22) *Gaussian 16 Rev. C.01*; Wallingford, CT, 2016. (accessed.
(23) Becke, A. D. Density-functional thermochemistry. III. The role of exact exchange. *J. Chem. Phys.* **1993**, *98* (7), 5648-5652.
(24) Ditchfield, R.; Hehre, W. J.; Pople, J. A. Self-Consistent Molecular-Orbital Methods. IX. An Extended Gaussian-Type Basis for Molecular-Orbital Studies of Organic Molecules. *J. Chem. Phys.* **1971**, *54* (2), 724-728.
(25) Rassolov, V. A.; Ratner, M. A.; Pople, J. A.; Redfern, P. C.; Curtiss, L. A. 6-31G* basis set for third-row atoms. *J. Comput. Chem.* **2001**, *22* (9), 976-984.
(26) Fuentealba, P.; Preuss, H.; Stoll, H.; Von Szentpály, L. A proper account of core-polarization with pseudopotentials: single valence-electron alkali compounds. *Chem. Phys. Lett.* **1982**, *89* (5), 418-422. Schwerdtfeger, P.; Dolg, M.; Schwarz, W. H. E.; Bowmaker, G. A.; Boyd, P. D. W. Relativistic effects in gold chemistry. I. Diatomic gold compounds. *J. Chem. Phys.* **1989**, *91* (3), 1762-1774.
(27) Scalmani, G.; Frisch, M. J. Continuous surface charge polarizable continuum models of solvation. I. General formalism. *J. Chem. Phys.* **2010**, *132* (11), 114110.
(28) Neese, F. Software update: The ORCA program system—Version 5.0. *WIREs Computational Molecular Science* **2022**, *12* (5), e1606. Neese, F. The ORCA program system. *WIREs Computational Molecular Science* **2012**, *2* (1), 73-78.
(29) Schäfer, A.; Horn, H.; Ahlrichs, R. Fully optimized contracted Gaussian basis sets for atoms Li to Kr. *J. Chem. Phys.* **1992**, *97* (4), 2571-2577.
(30) van Lenthe, E.; Snijders, J. G.; Baerends, E. J. The zero-order regular approximation for relativistic effects: The effect of spin–orbit coupling in closed shell molecules. *J. Chem. Phys.* **1996**, *105* (15), 6505-6516.
(31) Pantazis, D. A.; Chen, X.-Y.; Landis, C. R.; Neese, F. All-Electron Scalar Relativistic Basis Sets for Third-Row Transition Metal Atoms. *J Chem Theory Comput* **2008**, *4* (6), 908-919.
(32) Lin, Y.-S.; Li, G.-D.; Mao, S.-P.; Chai, J.-D. Long-Range Corrected Hybrid Density Functionals with Improved Dispersion Corrections. *J Chem Theory Comput* **2013**, *9* (1), 263-272.
(33) Martin, R. L. Natural transition orbitals. *J. Chem. Phys.* **2003**, *118* (11), 4775-4777.